AMERICAN SOCIETY FOR MICROBIOLOGY | Applied and Environmental Microbiology

Environmental Microbiology | Full-Length Text

UV-A radiation increases biomass yield by enhancing energy flow and carbon assimilation in the edible cyanobacterium *Nostoc sphaeroides*

Zhen Chen,[1] Zu-Wen Yuan,[1] Wei-Xin Luo,[1] Xun Wu,[1] Jin-Long Pan,[1] Yong-Qi Yin,[1] Hai-Chen Shao,[1] Kui Xu,[1] Wei-Zhi Li,[1] Yuan-Liang Hu,[1] Zhe Wang,[2] Kun-Shan Gao,[3] Xiong-Wen Chen[1]

AUTHOR AFFILIATIONS See affiliation list on p. 18.

ABSTRACT Ultraviolet (UV) A radiation (315–400 nm) is the predominant component of solar UV radiation that reaches the Earth's surface. However, the underlying mechanisms of the positive effects of UV-A on photosynthetic organisms have not yet been elucidated. In this study, we investigated the effects of UV-A radiation on the growth, photosynthetic ability, and metabolome of the edible cyanobacterium *Nostoc sphaeroides*. Exposures to 5–15 W m^{-2} (15–46 µmol photons m^{-2} s^{-1}) UV-A and 4.35 W m^{-2} (20 µmol photons m^{-2} s^{-1}) visible light for 16 days significantly increased the growth rate and biomass production of *N. sphaeroides* cells by 18%–30% and 15%–56%, respectively, compared to the non-UV-A-acclimated cells. Additionally, the UV-A-acclimated cells exhibited a 1.8-fold increase in the cellular nicotinamide adenine dinucleotide phosphate (NADP) pool with an increase in photosynthetic capacity (58%), photosynthetic efficiency (24%), Q_A re-oxidation, photosystem I abundance, and cyclic electron flow (87%), which further led to an increase in light-induced NADPH generation (31%) and ATP content (83%). Moreover, the UV-A-acclimated cells showed a 2.3-fold increase in ribulose-1,5-bisphosphate carboxylase/oxygenase activity, indicating an increase in their carbon-fixing capacity. Gas chromatography–mass spectrometry-based metabolomics further revealed that UV-A radiation upregulated the energy-storing carbon metabolism, as evidenced by the enhanced accumulation of sugars, fatty acids, and citrate in the UV-A-acclimated cells. Therefore, our results demonstrate that UV-A radiation enhances energy flow and carbon assimilation in the cyanobacterium *N. sphaeroides*.

IMPORTANCE Ultraviolet (UV) radiation exerts harmful effects on photo-autotrophs; however, several studies demonstrated the positive effects of UV radiation, especially UV-A radiation (315–400 nm), on primary productivity. Therefore, understanding the underlying mechanisms associated with the promotive effects of UV-A radiation on primary productivity can facilitate the application of UV-A for CO_2 sequestration and lead to the advancement of photobiological sciences. In this study, we used the cyanobacterium *Nostoc sphaeroides*, which has an over 1,700-year history of human use as food and medicine, to explore its photosynthetic acclimation response to UV-A radiation. As per our knowledge, this is the first study to demonstrate that UV-A radiation increases the biomass yield of *N. sphaeroides* by enhancing energy flow and carbon assimilation. Our findings provide novel insights into UV-A-mediated photosynthetic acclimation and provide a scientific basis for the application of UV-A radiation for optimizing light absorption capacity and enhancing CO_2 sequestration in the frame of a future CO_2 neutral, circular, and sustainable bioeconomy.

KEYWORDS cyanobacterium, growth, metabolome, *Nostoc sphaeroides*, photosynthesis, ultraviolet A radiation

Editor Gladys Alexandre, University of Tennessee at Knoxville, Knoxville, Tennessee, USA

Address correspondence to Xiong-Wen Chen, xwchen@hbnu.edu.cn.

The authors declare no conflict of interest.

See the funding table on p. 18.

Received 1 December 2023
Accepted 25 January 2024
Published 23 February 2024

The ultraviolet (UV) radiation that reaches the Earth's surface (UV-A: 315–400 nm and UV-B: 280–315 nm) comprises approximately 8%–9% of the total solar radiation, in terms of energy (1–3). Increased UV-B radiation due to ozone depletion has been widely reported to exert harmful effects on various photosynthetic organisms within the euphotic zone by damaging biological molecules and impairing physiological and biochemical processes (4–10). Although UV-A radiation is not attenuated by the ozone layer, it too has a substantial impact on primary productivity (11, 12). UV-A radiation exerts both positive and negative effects on photo-autotrophs; however, these effects are variable and are usually influenced by other environmental factors (5, 9, 13–20). For instance, high levels of UV-A radiation inhibit the photosynthetic productivity of cyanobacteria and algae, while low to moderate levels of UV-A radiation under low-light conditions drive photosynthetic carbon fixation in phytoplankton and macroalgae (17, 20, 21). Therefore, understanding the mechanisms underlying the positive effects of UV-A radiation on the primary productivity is significant for the application of UV-A for CO_2 sequestration and for promoting photobiological sciences.

Photosynthetic organisms can harvest UV-A energy and use it as environmental signals (22–29). Mechanistically, UV-A energy can be directly absorbed by chlorophyll (Chl) and carotenoids to drive photosynthetic electron transfer and carbon fixation, since these pigments exhibit partial absorption of the near UV range (22). Additionally, UV-A energy can be indirectly absorbed by photosynthetic pigments as UV-A-excited blue-green fluorescence emitted by phenolic compounds (13, 23–25). Furthermore, UV-A reportedly activates photoprotective responses by stimulating the synthesis of flavonoids, which scavenge hydrogen peroxide and singlet oxygen generated under excess light stress (26–29). On the other hand, in response to external light cues in the range from 300 to 750 nm, photosynthetic organisms can tune the synthesis of pigments and photosystems (PSs) to improve light harvesting and energy conversion (30). However, the UV-A-mediated acclimation response of the photosynthetic apparatus remains unclear.

Cyanobacteria are the oldest lineage of oxygenic photosynthetic organisms, and they contribute to at least 25% of global primary productivity (31). They thrive in every illuminated environment, including aquatic system and terrestrial systems as well as extreme environments (32), with UV radiation being a key ecological factor in their habitats (33). Several studies have documented the deleterious effects of UV radiation and the associated defensive mechanisms in cyanobacterium (8). Although the detrimental effects of UV radiation on living organisms are generally attributed to UV-B radiation, many cellular processes are also affected by UV-A radiation (8, 9). In *Nostoc punctiforme* ATCC 29133, UV-A radiation specifically induces the synthesis of scytonemin, which accumulates at the extracellular sheath (34), while in some motile cyanobacteria, UV-A radiation activates multiple phototaxis signaling pathways to trigger movement away from high levels of solar radiation in some motile cyanobacteria (35).

Nostoc sphaeroides is an edible and medicinal cyanobacterium (36) that primarily grows in the mountainous paddy fields of Southern and Central China and forms spherical macro-colonies of up to 2-cm diameter (37). In a previous study, we sequenced the complete genome of *N. sphaeroides* CCNUC1 and deciphered its ecological adaptation to the highly dynamic paddy-field habitat at genomic and transcriptomic levels (38). Additionally, we also demonstrated its positive responses and photosynthetic acclimation mechanism to low-dose UV-B radiation (38, 39). Since UV-A radiation is a crucial ecological factor in paddy fields, it may also exert positive effects on the productivity of *N. sphaeroides*. Therefore, in this study, we examined the effects of UV-A radiation on the growth, photosynthetic ability, and metabolome of *N. sphaeroides* CCNUC1. Our results demonstrated that UV-A radiation increased the biomass yield of *N. sphaeroides* CCNUC1 by regulating photosynthetic activity and metabolism.

RESULTS

UV-A radiation promoted the growth of *N. sphaeroides* under low-light conditions

N. sphaeroides CCNUC1 showed a decreased growth rate under high levels of UV-A radiation and an increased growth rate under low to moderate levels of UV-A at 4.35 W m^{-2} photosynthetically active radiation (PAR; 20 µmol photons m^{-2} s^{-1}; Fig. 1A). UV-A

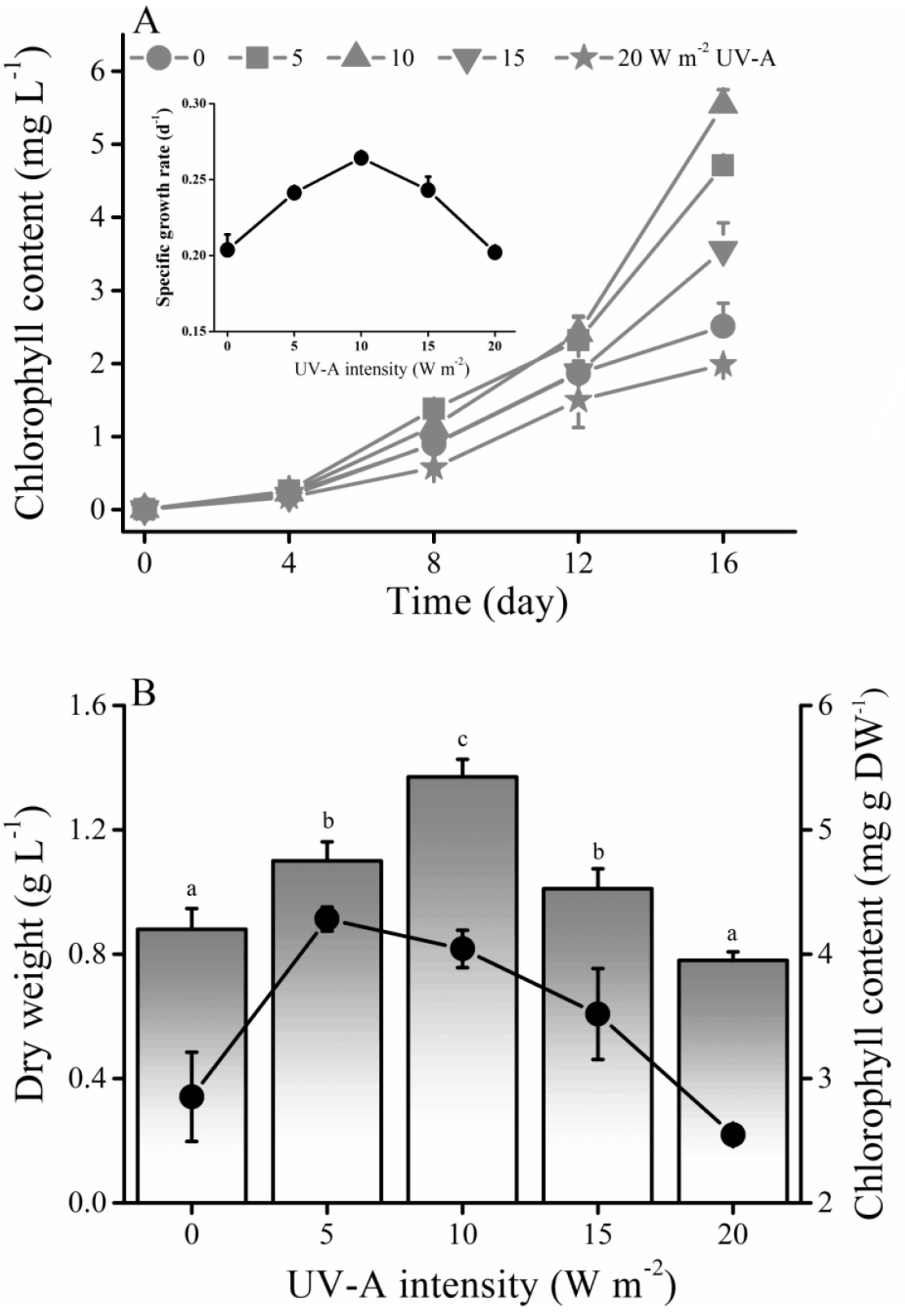

FIG 1 Effects of UV-A radiation on the growth of *N. sphaeroides* CCNUC1 under 4.35 W m^{-2} PAR. (A) Growth curves based on the Chl content under different intensities of UV-A radiation (n = 3–4). (B) Biomass accumulation of *N. sphaeroides* CCNUC1 after 16 days of exposure to different intensities of UV-A radiation under 4.35 W m^{-2} PAR (n = 5). Columns represent DW (g L^{-1}), and solid black circles represent Chl content (mg g DW^{-1}). Values marked with different subscript letters are significantly different (Tukey's HSD, $P < 0.05$), whereas values marked with the same subscript letter are not. Data are presented as means ± standard deviation.

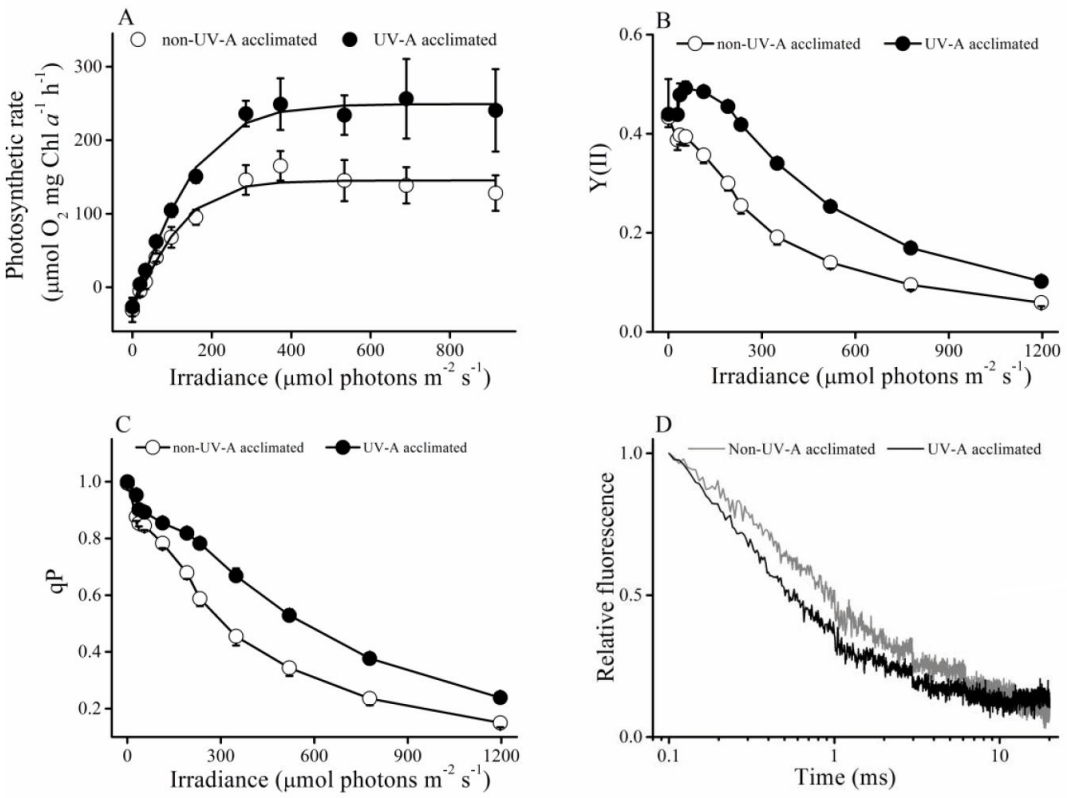

FIG 2 PSII function in *N. sphaeroides* CCNUC1 after 16 days of exposure to 10 W m^{-2} UV-A radiation and 4.35 W m^{-2} PAR. (A) *P–I* response curves of the non-UV-A-acclimated (control; open circle) and UV-A-acclimated (solid circle) cells (n = 4–5). (B) PSII effective photochemical efficiency [Y(II)]–irradiance response curves of the control (open circle) and UV-A-acclimated cells (solid circle) (n = 4–8). (C) PSII photochemical quenching coefficient (*qP*)–irradiance response curves of the control (open circle) and UV-A-acclimated cells (solid circle) (n = 5–8). (D) Chl fluorescence decay in the control (gray trace) and UV-A-acclimated (black trace) cells (n = 5). Variable fluorescence was induced by a saturating single turnover flash. Data are presented as means ± standard deviation.

radiation at <20 W m^{-2} (60 µmol photons m^{-2} s^{-1}) had a significant positive effect on the growth rate of *N. sphaeroides* CCNUC1. For instance, exposure to 5, 10, and 15 W m^{-2} UV-A radiation (15, 30, and 46 µmol photons m^{-2} s^{-1}) significantly increased the growth rate of *N. sphaeroides* CCNUC1 by 18%, 30%, and 19% [Tukey's honestly significant difference (HSD), $P < 0.001$], respectively, and its biomass yield by 25%, 56%, and 15%, respectively (Tukey's HSD, $P < 0.05$; Fig. 1A and B). Additionally, exposure to 5, 10, and 15 W m^{-2} UV-A radiation significantly increased the Chl content of *N. sphaeroides* CCNUC1

TABLE 1 Photosynthetic parameters of *N. sphaeroides* CCNUC1 after 16 days of exposure to 10 W m^{-2} UV-A radiation and 4.35 W m^{-2} PAR[a]

Parameters	Non-UV-A acclimated	UV-A acclimated
P_{max} (µmol O_2 mg Chl a^{-1} h^{-1})	174.28 ± 18.15	275.23 ± 33.71**
α (µmol O_2 mg Chl a^{-1} h^{-1}) (µmol m^{-2} s^{-1})$^{-1}$	1.13 ± 0.05	1.40 ± 0.13**
F_v/F_{mDCMU}	0.41 ± 0.05	0.39 ± 0.01^{ns}
PSII activity (H_2O → *p*-BQ) (µmol O_2 mg Chl a^{-1} h^{-1})	168.45 ± 39.14	161.03 ± 33.82^{ns}
t_1 (ms)	0.58 ± 0.04	0.32 ± 0.05***
t_2 (ms)	7.68 ± 2.62	2.27 ± 0.35**

[a]The light-saturated photosynthetic rate (P_{max}) and the light-limited photosynthetic efficiency (α) were derived from photosynthetic response to irradiance (*P–I*) curves (Fig. 2A). The maximal PSII photochemical quantum yield (F_v/F_{mDCMU}) was calculated from fluorescence measurements of dark-adapted cells in the presence of 20-µM DCMU. The PSII activity was determined at 550 µmol photons m^{-2} s^{-1} with H_2O as the electron donor and *p*-BQ as the electron acceptor in the presence of 1-mM *p*-BQ and 1-mM potassium ferricyanide. Lifetimes of the fast (t_1) and slower phase (t_2) of Q_A^- re-oxidation were obtained after fitting the fluorescence decay curves (Fig. 2D) by a sum of two exponential function. Statistical significance of the same parameter was analyzed using *t*-test at $^{*}P < 0.05$, $^{**}P < 0.01$, $^{***}P < 0.001$, and ns (no significant difference) $P > 0.05$. Data are means ± standard deviation (n = 3–5).

by 50%, 42%, and 23%, respectively (Tukey's HSD, $P < 0.05$; Fig. 1B). We further investigated the effects of PAR intensity on the productivity of *N. sphaeroides* CCNUC1 under 10 W m^{-2} UV-A radiation. The results revealed that UV-A radiation significantly increased the biomass yield of *N. sphaeroides* CCNUC1 by approximately 55% at <50 µmol photons m^{-2} s^{-1} PAR but significantly decreased the biomass yield by 9%–23% at >50 µmol photons m^{-2} s^{-1} PAR (*t*-test, $P < 0.001$; Fig. S1). To gain further insights into the positive effects of UV-A radiation on the productivity of *N. sphaeroides* CCNUC1, we investigated its photosynthetic ability and metabolome at 10 W m^{-2} UV-A radiation (30 µmol photons m^{-2} s^{-1}) under 4.35 W m^{-2} PAR (20 µmol photons m^{-2} s^{-1}).

UV-A radiation enhanced the photosynthetic capacity and Q_A re-oxidation ability of *N. sphaeroides*

The effects of UV-A radiation on the photosynthetic activity of *N. sphaeroides* CCNUC1 are presented in Fig. 2 and Table 1. Photosynthetic–irradiance (*P–I*) response curves showed that compared to the non-UV-A-acclimated *N. sphaeroides* CCNUC1 (control), the photosynthetic rate of UV-A-acclimated *N. sphaeroides* CCNUC1 increased more rapidly with an increase in light intensity (Fig. 2A). Additionally, the photosynthetic efficiency (α) and photosynthetic capacity (P_{max}) of the UV-A-acclimated cells increased by 24% (*t*-test, $P < 0.01$) and 58% (*t*-test, $P < 0.01$), respectively, compared to the control cells (Fig. 2A; Table 1). The light response curves of the PSII effective photochemical efficiency [Y(II)] showed that with an increase in irradiance, the Y(II) values of the control cells decreased gradually down to 0.06 at 1,197 µmol photons m^{-2} s^{-1}, while the Y(II) values of the UV-A-acclimated cells first increased slightly at <200 µmol m^{-2} s^{-1} and then decreased gradually down to 0.1 at 1,197 µmol m^{-2} s^{-1} (Fig. 2B). Moreover, the light response curves of the PSII photochemical quenching coefficient (*qP*) showed that with an increase in irradiance, the *qP* values of the UV-A-acclimated cells declined more gradually than that of control cells, reaching 0.24 and 0.15, respectively, at 1,197 µmol m^{-2} s^{-1} (Fig. 2C). These results indicate that acclimation to UV-A radiation enhanced the photosynthetic capacity of *N. sphaeroides* CCNUC1. However, the PSII activity from H_2O to plastoquinone and the maximum PSII photochemical efficiency (F_v/F_m) showed no significant differences between UV-A acclimated and control cells (Table 1).

To further investigate the effects of UV-A radiation on PSII function, the kinetics of Q_A^- re-oxidation were analyzed by determining the fluorescence decay (Fig. 2D), which reflects the re-oxidation of Q_A via forward electron transport to Q_B (and Q_B^-) by the lifetimes of different phases, fast phase (t_1) and slow phase (t_2) (40). As shown in Fig. 2D; Table 1, acclimation to UV-A radiation led to a significant decline in the lifetimes of the t_1 and t_2 phases by 46% and 70%, respectively, in *N. sphaeroides* CCNUC1 (*t*-test, $P < 0.01$). These results indicate that Q_A re-oxidation was more rapid in the UV-A-acclimated *N. sphaeroides* CCNUC1.

UV-A radiation increased PSI abundance and cyclic electron transfer in *N. sphaeroides*

The effects of UV-A radiation on the PSI function of *N. sphaeroides* CCNUC1 are shown in Fig. 3A. The maximum amount of photo-oxidizable P700 (Pm; representing the quantity of efficient PSI complex) in UV-A-acclimated cells increased significantly by 37% compared to the control cells (*t*-test, $P < 0.01$), suggesting that acclimation to UV-A radiation increased the oxidizing photochemical activity of PSI. To determine the nature of the enhanced PSI oxidizing capacity, we performed Western blot analysis against core PSII (D1 and CP47) and PSI (PsaA/B and PsaC) subunits for the control and UV-A-acclimated cells. The D1 and CP47 contents showed no significant changes (*t*-test, $P > 0.05$), but PsaA/B and PsaC contents increased significantly by 30% and 25%, respectively, in the UV-A-acclimated cells (*t*-test, $P < 0.001$), compared to the control cells (Fig. 3B; Fig. S2). These results indicate that UV-A radiation-induced the enhancement of PSI abundance in *N. sphaeroides* CCNUC1.

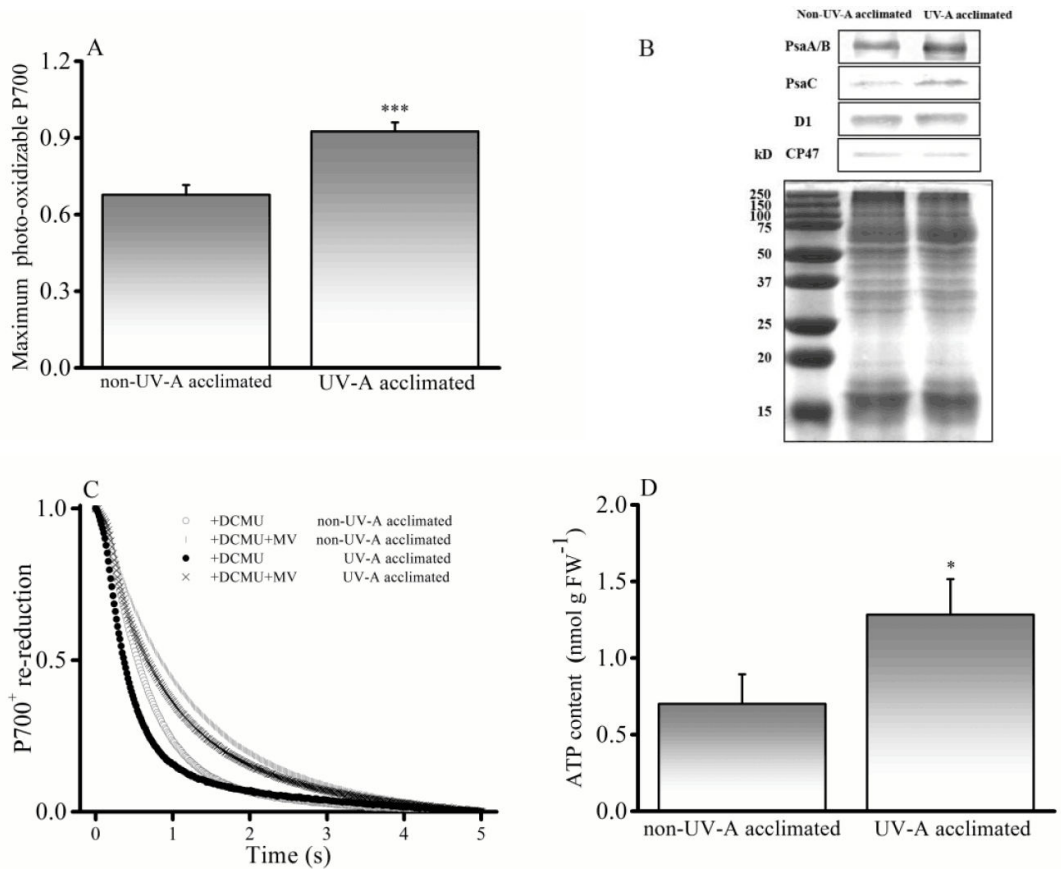

FIG 3 PSI function in *N. sphaeroides* CCNUC1 after 16 days of exposure to 10 W m^{-2} UV-A radiation and 4.35 W m^{-2} PAR. (A) Maximum photo-oxidizable P700 (Pm) of *N. sphaeroides* CCNUC1 was determined through the application of a saturation pulse after far-red pre-illumination for 10 s (n = 4). (B) Core proteins of PSI (PsaA/B and PsaC) and PSII (D1 AND CP47). Membrane proteins (10 µg) of non-UV-A acclimated and UV-A acclimated cells were separated by SDS-PAGE (lower panel) and subjected to Western blotting (upper panel) probed with D1-, CP47-, PsaA/B-, and PsaC-specific antibodies. (C) $P700^+$ reduction curves of *N. sphaeroides* CCNUC1 in darkness after turning off far-red light treated with DCMU and MV; 20-µM DCMU was used to disrupt the linear electron flow; 2-mM MV was used as an efficient PSI electron acceptor to block the CEF. The curves are normalized to the maximal signal (n = 3–4). (D) The ATP contents in the control and UV-A-acclimated cells (n = 3). Statistical significance of the same parameter was analyzed using t-test at $^*P < 0.05$, $^{**}P < 0.01$, and $^{***}P < 0.001$. Data are presented as means ± standard deviation.

The $P700^+$ dark reduction kinetics were also monitored in *N. sphaeroides* CCNUC1 (Fig. 3C), after turning off the far-red light. The $P700^+$ reduction rate constants were determined from the calculated electron transfer rate (Table 2). The linear electron transfer through PSII was blocked using 3-(3,4-dichlorophenyl)-1,1-dimethylurea (DCMU). The $P700^+$ reduction kinetics in the presence of DCMU represent the electrons derived from cyclic and respiratory electron flow. Since far-red light was provided for preferential excitation of PSI, no significant differences were observed in the $P700^+$ reduction rate

TABLE 2 Rate constants for $P700^+$ reduction of *N. sphaeroides* CCNUC1 treated with DCMU and MV after 16 days of exposure to 10 W m^{-2} UV-A radiation and 4.35 W m^{-2} PAR[a]

	$P700^+$ reduction rate (k, s^{-1})	
Inhibitors used	**Non-UV-A acclimated**	**UV-A acclimated**
(1) +DCMU (CEF + Res)	1.28 ± 0.11	1.88 ± 0.05***
(2) +DCMU + MV (Res)	0.82 ± 0.06	1.03 ± 0.09*
(1) – (2) (CEF)	0.46 ± 0.06	0.85 ± 0.09***

[a]Twenty-micromolar DCMU and 2-mM MV were used to disrupt the linear electron flow and the CEF, respectively. Res: the electrons flowing through PSI derived from the respiratory electron transport chain. Statistical significance of the same parameter was analyzed using t-test at $^*P < 0.05$, $^{**}P < 0.01$, and $^{***}P < 0.001$. Data are means ± standard deviation (n = 3–4).

constant of UV-A-acclimated and the control cells in the presence or absence of DCMU (data not shown), while in the presence of DCMU, the $P700^+$ reduction rate of the UV-A-acclimated cells increased significantly by 47% (*t*-test, $P < 0.01$) compared to the control cells. Methyl viologen (MV) blocks the cyclic electron flow (CEF) around PSI (41), and the $P700^+$ reduction kinetics in the presence of both DCMU and MV represents the electrons flowing through PSI derived from the respiratory electron flow. In the presence of both DCMU and MV, the $P700^+$ reduction rate in the UV-A-acclimated samples increased by 26% (*t*-test, $P = 0.01$), compared to that in the control cells (Fig. 3C; Table 2). To determine the CEF, we calculated the difference between $P700^+$ re-reduction in the presence and absence of MV and found that the $P700^+$ reduction rate increased by 85% in the UV-A-acclimated cells (*t*-test, $P < 0.01$). Since CEF is important for driving ATP synthesis, we calculated the ATP content in *N. sphaeroides* CCNUC1 (Fig. 3D). The results revealed that the ATP content in the UV-A-acclimated cells increased by 83% compared to that in the control cells. These results indicate that UV-A radiation significantly upregulated CEF and ATP synthesis in *N. sphaeroides* CCNUC1.

UV-A radiation upregulated NADP(H) pool and Rubisco activity in *N. sphaeroides*

Nicotinamide adenine dinucleotide phosphate [NADP(H)] is the driving force of anabolism and biomass accumulation (42), the NADPH content and the NADP pool (sum of $NADP^+$ and NADPH) in *N. sphaeroides* CCNUC1 were determined under UV-A radiation (Fig. 4A and B), and the results revealed that the NADPH content and the NADP pool size increased by 2.2-fold (*t*-test, $P < 0.01$) and 1.8-fold (*t*-test, $P = 0.02$), respectively, in the UV-A-acclimated cells, compared to those in the control cells. Furthermore, light-induced NADPH generation was assessed by measuring the dark–light–dark induction transients of NADPH fluorescence. At the onset of actinic light, light-induced NADPH fluorescence increased rapidly by 31% in the UV-A-acclimated cells compared to that in the control cells (*t*-test, $P = 0.03$), indicating that light-driven generation of NADPH is higher in the UV-A-acclimated cells. Subsequently, the NADPH fluorescence declined in both UV-A-acclimated and control cells due to NADPH oxidation via downstream metabolic pathways and gradually reached a stationary phase, corresponding to the matching rates of light-driven $NADP^+$ reduction and NADPH oxidation (43). The NADPH fluorescence declined by 51% and 18%, respectively, in the UV-A-acclimated and control cells (*t*-test, $P = 0.04$), indicating that in the UV-A-acclimated cells, the NADPH consumption increases more significantly owing to the downstream metabolic pathways and biomass accumulation. After the actinic light was switched off, NADPH fluorescence immediately further decreased, and the decrease extent in UV-A acclimated cells was 26% more than that of the control cells (*t*-test, $P = 0.04$), indicating that the dark oxidation of NADPH was higher in the UV-A-acclimated cells. Finally, NADPH fluorescence increased gradually to a stable value, corresponding to the matching rates of dark oxidation of NADPH and dark reduction of $NADP^+$ associated with reductive pentose phosphate cycle.

During the dark–light–dark induction transients of NADPH fluorescence, NADPH is primarily consumed by the Calvin cycle (43). Therefore, we assessed the effect of UV-A radiation on the enzyme activity of ribulose-1,5-bisphosphate carboxylase/oxygenase (Rubisco) in *N. sphaeroides* CCNUC1 (Fig. 4C). The results revealed that the UV-A-acclimated cells exhibited a 2.3-fold increase in Rubisco activity compared to the control cells (*t*-test, $P < 0.01$), suggesting that UV-A radiation might boost carbon fixing and downstream carbon metabolism in *N. sphaeroides* CCNUC1 to increase its NADPH consumption.

UV-A radiation promoted the accumulation of energy-storing carbon metabolites in *N. sphaeroides*

To explore the metabolic responses to the increase in ATP and NADPH contents under UV-A radiation, we conducted gas chromatography–mass spectrometry (GC–MS)-based metabolomics in *N. sphaeroides* CCNUC1. The multivariate orthogonal partial least

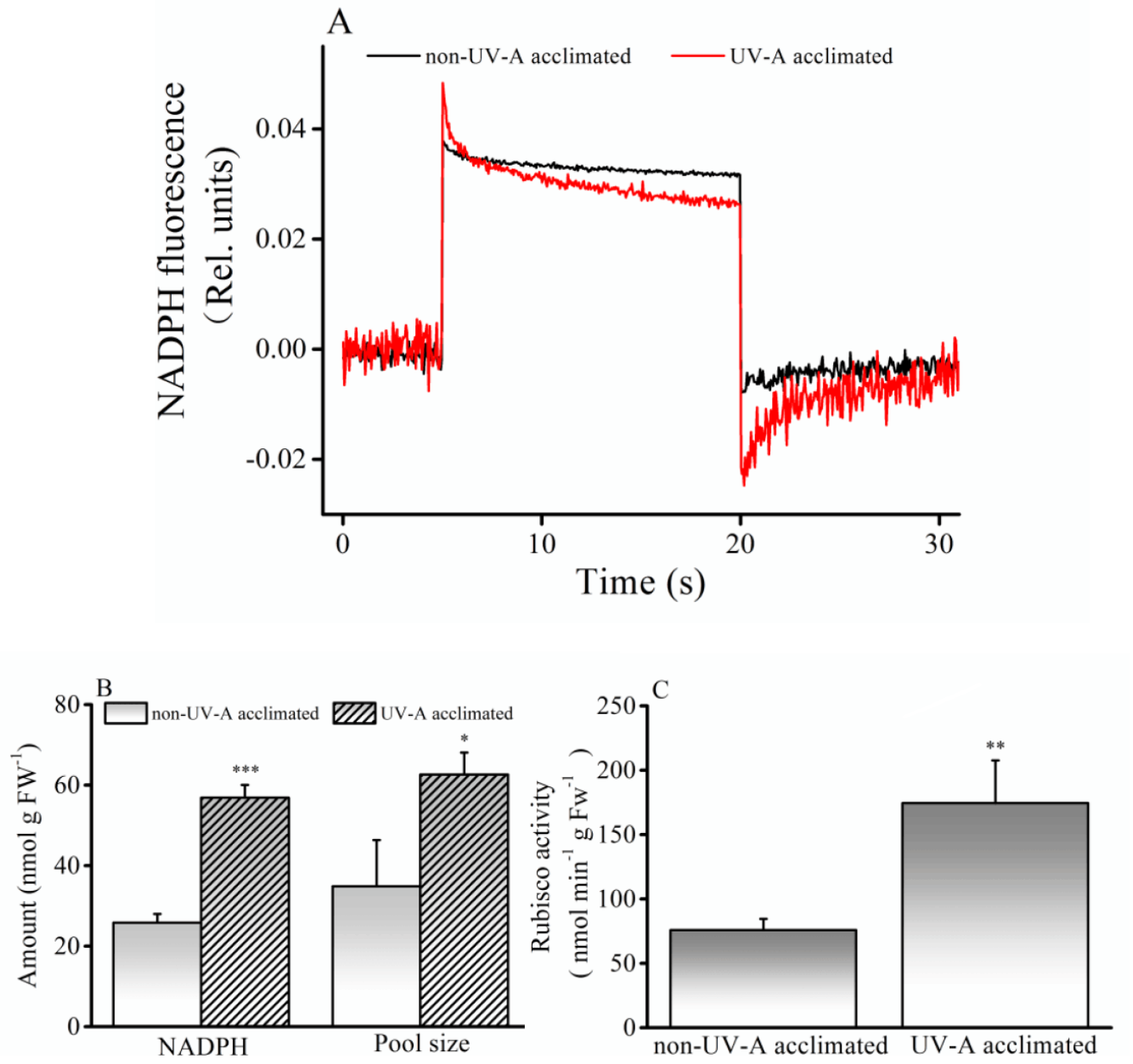

FIG 4 NADP(H) generation and Rubisco activity in *N. sphaeroides* CCNUC1 after 16 days of exposure to 10 W m^{-2} UV-A radiation and 4.35 W m^{-2} PAR. (A) The dark–light–dark induction kinetics of NADPH fluorescence in the non-UV-A-acclimated (control; black) and UV-A-acclimated (red) cells (n = 3). The samples were repetitively illuminated (15-s light/10-s dark intervals), and the values were calculated as an average of 10 dark–light–dark cycles. (B) The NADPH content and the size of NADP pool (sum of $NADP^+$ and NADPH) in the control and UV-A-acclimated cells (n = 3). (C) Rubisco activity in the control and UV-A-acclimated cells (n = 3). Data are presented as means ± standard deviation. Statistical significance of the same parameter was analyzed using t-test at $^*P < 0.05$, $^{**}P < 0.01$, and $^{***}P < 0.001$.

squares discriminant analysis (OPLS-DA) of metabolomic data revealed that acclimation to UV-A radiation altered the metabolite profile of *N. sphaeroides* CCNUC1 (Fig. S3). We detected a total of 262 metabolites in *N. sphaeroides* CCNUC1, among which 64 metabolites were significantly altered [$P < 0.05$; >1.5-fold changes; variable importance of projection (VIP) > 1], consisting of 25 significantly upregulated and 39 significantly downregulated metabolites (Fig. S4; Table S1). The "organic oxygen compounds" accounted for the highest proportion (31%) of the significantly altered metabolites, followed by "lipids and lipid-like molecules" (15%), "organic acids and derivatives" (13%),

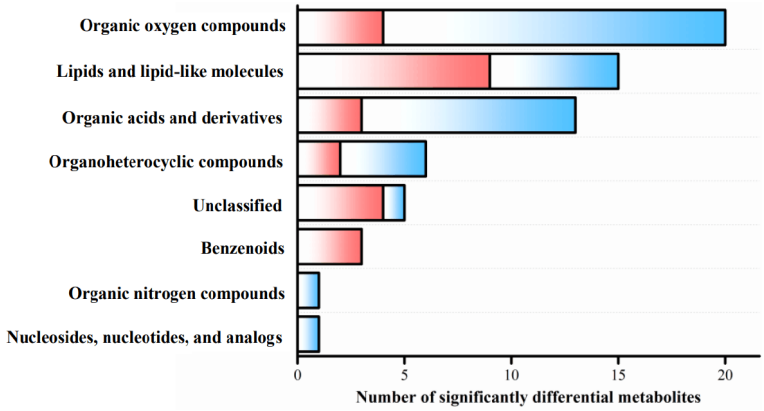

FIG 5 Significantly differential metabolites between the non-UV-A-acclimated and UV-A-acclimated *N. sphaeroides* CCNUC1 cells after 16 days of exposure to 10 W m^{-2} UV-A radiation and 4.35 W m^{-2} PAR. Metabolites were analyzed by GC–MS (n = 6) and classified by chemical taxonomy according to the Human Metabolome Database. Pink represents significantly upregulated metabolites, and blue represents significantly downregulated metabolites. Data are presented as means ± standard deviation.

and other metabolites of smaller proportions, such as "organoheterocyclic compounds" and "benzenoids" (Fig. 5).

Significantly differential metabolites associated with central carbon metabolism are shown in Fig. 6. The results revealed that in the Calvin cycle, phosphorylated sugars, such as ribulose 5-phosphate, fructose 6-phosphate, and its interconvertible analogs glucose 6-phosphate, galactose 6-phosphate, and mannose 6-phosphate, were significantly decreased, while sugars, such as galactose, fructose, and lactose, were significantly increased (Fig. 6A). Additionally, pyruvate (a biomarker of glycolysis) was significantly downregulated, while several acetyl-coA-derived fatty acids, such as caproic acid, behenic acid, lignoceric acid, and arachidic acid, were significantly increased (t-test, $P < 0.01$). Moreover, in tricarboxylic acid cycle, the citrate content was significantly increased in the UV-A-acclimated cells (t-test, $P < 0.01$; Fig. 6B). The significant accumulation of sugars and lipids suggested that UV-A radiation boosted energy-storing carbon metabolism (Fig. 7).

Amino acid metabolism is closely associated with central carbon metabolism. In this study, we found nine significantly altered amino acids, among which L-methionine was significantly upregulated, while other amino acids, such as L-asparagine, L-glutamine, and L-cysteine, were significantly downregulated in the UV-A-acclimated cells (Fig. 6C and 7).

DISCUSSION

A novel mechanism of photosynthetic acclimation to UV-A radiation

Although UV radiation has been largely found to negatively affect photosynthesis, a few studies have reported the positive effects of UV, especially those of UV-A (315–400 nm) on photosynthesis (5, 9, 13, 14, 17, 18). Exposure to UV-A radiation at <20 W m^{-2} (60 µmol photons m^{-2} s^{-1}) drives photosynthetic CO_2 fixation in larger-sized phytoplankton under reduced or rapidly fluctuating solar radiation (9, 17, 20, 21). In this study, we observed that exposure to 5–15 W m^{-2} (15–46 µmol photons m^{-2} s^{-1}) UV-A and 4.35 W m^{-2} (20 µmol photons m^{-2} s^{-1}) PAR significantly promoted biomass accumulation in *N. sphaeroides* CCNUC1. This may be because UV-A radiation can be directly absorbed by Chl as well as indirectly absorbed by photosynthetic pigments as UV-A-excited blue-green fluorescence emitted by phenolic compounds (14, 23–25) or by UV-A absorbing compounds, such as mycosporine-like amino acids and scytonemin (17, 44–46). In *N. sphaeroides* CCNUC1, UV-A energy at 365 nm was also confirmed to be utilized to excite the PSI and PSII fluorescence (Fig. S5). Our findings further

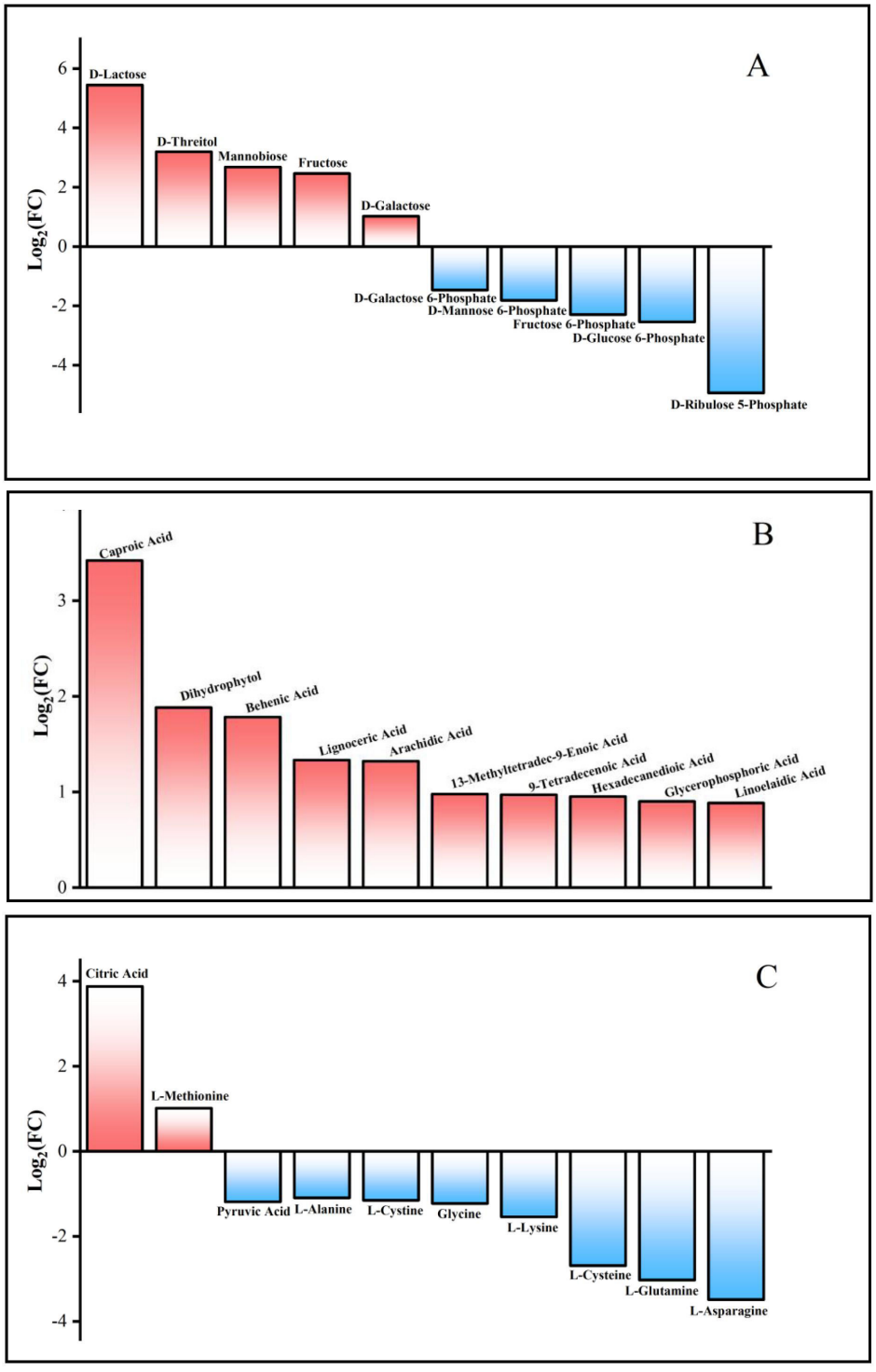

FIG 6 Carbon metabolism-related significantly differential metabolites in *N. sphaeroides* CCNUC1 after 16 days of exposure to 10 W m^{-2} UV-A radiation and 4.35 W m^{-2} PAR. (A–C) Box plot showing the relative abundance of Calvin cycle- and tricarboxylic acid cycle-associated carbohydrates and conjugates (A), lipids and lipid-like molecules (B), organic acids, and amino acids (C) in the UV-A-acclimated cells (n = 6). Pink represents significantly upregulated metabolites, and blue represents significantly downregulated metabolites.

suggest that acclimation to UV-A radiation alters photosynthetic activity and reprograms metabolism to exert positive effects on *N. sphaeroides* CCNUC1 productivity. In this study,

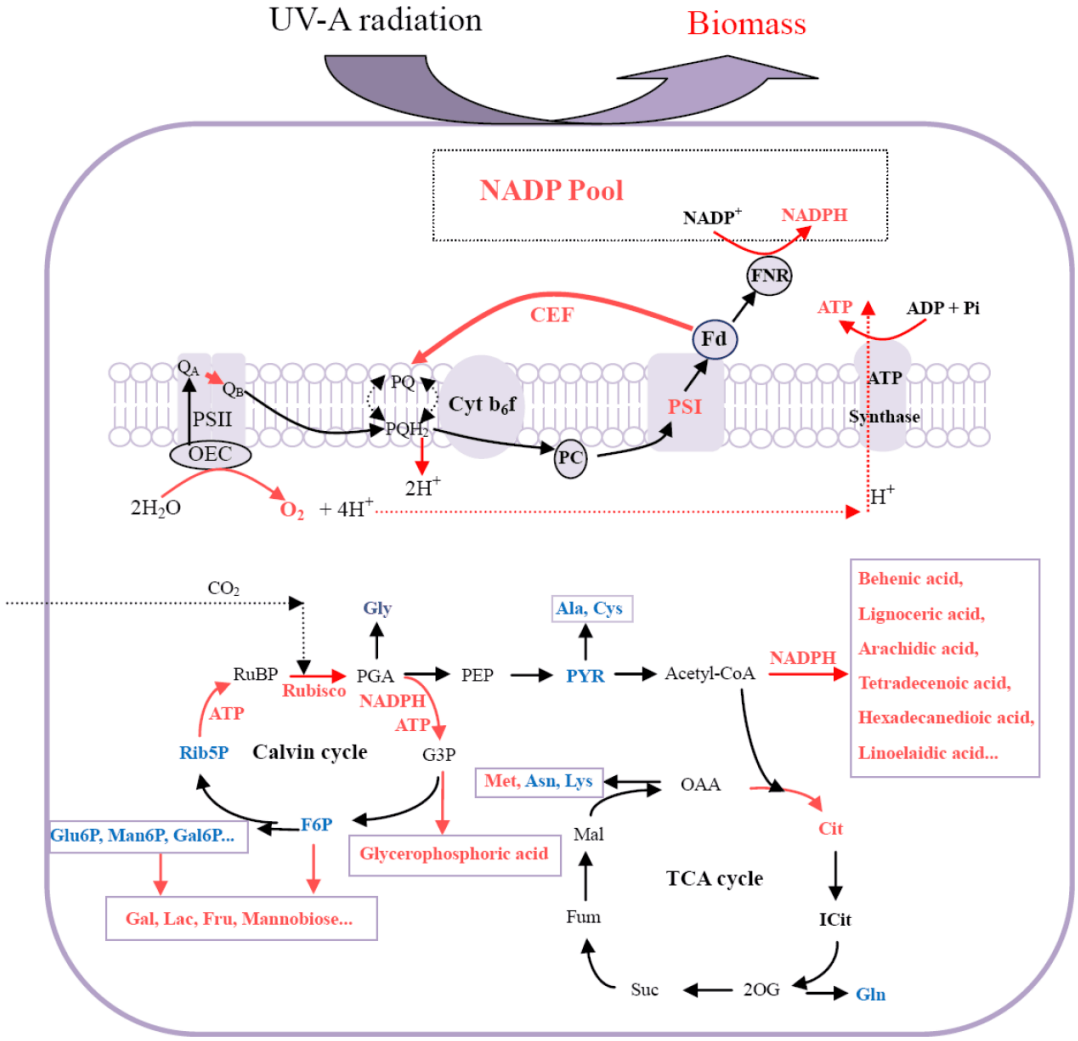

FIG 7 Schematic illustration of photosynthetic acclimation of *N. sphaeroides* CCNUC1 to UV-A radiation. Acclimation to UV-A radiation increases biomass yield via enhancing energy flow and carbon assimilation under low-light conditions, as indicated by the upregulation of NADP(H) generation with an increase in PSI abundance, CEF, and energy-storing carbon metabolism in *N. sphaeroides* CCNUC1. Metabolic pathways involved in carbon metabolism in *N. sphaeroides* CCNUC1 were generated by mapping labeled metabolites into known metabolic pathways. The arrows show the direction of the reaction. Pink represents significantly upregulated metabolites, and blue represents significantly downregulated metabolites. 2OG, 2-oxoglutarate; Ala, alanine; Asn, asparagine; Cit, citrate; Cys, cystine; Cyt b_6f, cytochrome b_6f complex; F6P, D-fructose-6-phosphate; Fd, ferredoxin; FNR, ferredoxin-NADP$^+$ reductase; Fru, fructose; Fum, fumarate; G3P, glyceraldehyde-3-phosphate; Gal, galactose; Gal6P, galactose 6-phosphate; Gln, glutamine; Glu6P, glucose 6-phosphate; Gly, glycine; ICit, isocitrate; Lac, lactose; Lys, lysine; Mal, malate; Man6P, mannose 6-phosphate; Met, methionine; OAA, oxaloacetate; OEC, oxygen evolving complex; PC, plastocyanin; PEP, phosphoenolpyruvate; PGA, 3-phosphoglyceric acid; PQ, plastoquinone; PYR, pyruvate; Q_A, primary quinone-type acceptor; Rib5P, ribulose 5-phosphate; Rubisco, ribulose-1,5-bisphosphate carboxylase/oxygenase; RuBP, ribulose 1,5-bisphosphate; Suc, succinate; TCA cycle, tricarboxylic acid cycle.

we found that *N. sphaeroides* CCNUC1 utilized UV-A radiation by increasing energy flow and enhancing carbon assimilation, as indicated by the upregulated NADPH generation with increased PSI abundance, CEF, and energy-storing carbon metabolism.

The NADP(H) content plays an essential role in the photosynthesis and growth of oxygenic photosynthetic organisms (47–50). NADP$^+$ acts as the final acceptor of the photosynthetic electron transport chain and receives electrons via PSI for the generation of NADPH. Therefore, an enhanced supply of NADP pool provides more NADP$^+$ for the PSI acceptor side, contributing to increased NADPH production. In this study, a significant increase in the NADP pool was accompanied by an increase in light-induced NADPH generation and cellular NADPH content in the UV-A-acclimated *N. sphaeroides* CCNUC1. A decrease of NADP(H) pool impaired Chl synthesis and reduced

photosynthetic efficiency in a NAD kinase2 (NADK2) knockout mutant of *Arabidopsis* (47), while an increase in NADP(H) pool increased photosynthetic efficiency and oxidative damage tolerance in a NADK2-overexpressing mutant of rice (*Oryza sativa*) (48). Notably, $NADP^+$ supply regulates PSI synthesis in *Arabidopsis* chloroplasts (51), and a large pool of NADP(H) increases PSI content, photosynthetic efficiency, and growth of the cyanobacterium *Synechococcus elongatus* 2973 (52–54). Therefore, the results of our study indicate that the significant increase in NADP(H) pool, induced by UV-A radiation, plays a crucial regulatory role in enhancing PSI abundance, photosynthesis, and growth of *N. sphaeroides* CCNUC1.

Optimized stoichiometric quantity of PSI can not only protect PSI from photoinhibition but can also ensure robust photosynthesis (55). The enhancement of PSI abundance can alleviate the photosynthetic electron transport chain bottleneck and provide greater oxidizing power to accelerate electron transfer from PSII, thereby promoting photosynthetic capacity (39, 53, 56). In the present study, UV-A-acclimated cells showed an increase in P_{max}, PSI abundance, and Pm, which might serve to pull electrons from PSII more efficiently, as evidenced by the more rapid Q_A re-oxidation. Enhanced Q_A re-oxidation may also be attributed to cyclic PSII electron transport (57), whereas Q_A re-oxidation curves in the presence of DCMU showed no differences between the UV-A acclimated and control cells (Fig. S6); therefore, faster electron pulling from PSII in the UV-A acclimated cells may be due to the increase in both PSI abundance and Pm. The regulation of PSI abundance is an acclimation strategy for cyanobacterial survival under different environmental conditions (30). Iron deficiency or manganese limitation induced cyanobacteria to decrease the PSI content to balance electron transport rates between the PSs (58–60). In cyanobacteria, acclimation to high-light conditions leads to the downregulation of PSI content to avoid absorbing excessive light (61, 62), while acclimation to low-light conditions leads to increased Chl content and PSI abundance to promote light absorption (62, 63). Notably, UV-A or low UV-B (39) acclimation can further induce the PSI accumulation under low visible light conditions, indicating the presence of unidentified signal transduction components that integrate UV-A, UV-B, and low-light signaling, which need further investigation using multi-omic, genetic, and biochemistry technology in the future.

The regulation of CEF around PSI (CEF) is an adaptation strategy for coping with environmental changes and variable demand for ATP and NADPH (64, 65). Linear electron transport generates both ATP and NADPH, whereas PSI CEF generates a proton motive force for ATP synthesis. Moreover, PSI CEF is essential for balancing the ATP/NADPH production ratio to protect PSI and PSII from stromal over-reduction-induced damage under different environment conditions (66, 67). Therefore, considering the stoichiometric balancing of ATP and NADPH demand, the significant increase in NADPH generation must be one of the important reasons for the upregulation of PSI CEF in the UV-A-acclimated cells. CEF plays a crucial role in the growth of cyanobacteria under low-light conditions. For instance, under low-light conditions, *Synechococcus* sp. PCC 7002 mutants lacking CEF show a slower growth than the wild type (41). Therefore, the results of our study indicate that the upregulation of CEF in the UV-A acclimated *N. sphaeroides* CCNUC1 leads to increased ATP production for Chl synthesis and PSI accumulation to enhance light harvesting capacity and CO_2 assimilation under low-light conditions.

UV-A radiation could boost energy-storing carbon metabolism

Energy balance is important for improving photosynthetic productivity, ATP and NADPH play crucial roles in energy metabolism, and NADPH and ATP consumption of downstream metabolism should match NADPH and ATP supply from enhanced photosynthetic efficiency (68, 69). In photosynthetic cells, NADPH and ATP produced via the light reactions of photosynthesis are important driving force of the Calvin cycle for CO_2 assimilation (70). Therefore, in this study, an increase in light-induced NADPH generation and ATP content was accompanied by enhanced Rubisco activity and carbohydrate

accumulation in the UV-A-acclimated cells. NADPH plays a crucial role in long-chain fatty acid synthesis (71, 72), and an increase in NADPH supply can lead to higher lipid productivity and rapid growth of algal cells under high-CO_2 conditions (73). In engineered microbial cells, increased NADPH supply can enhance the production of some amino acids, such as L-methionine, L-arginine, and L-lysine (74, 75). Similarly, in this study, we observed the accumulation of sugars, long-chain fatty acids, and L-methionine in the UV-A-acclimated *N. sphaeroides* CCNUC1 cells, which can be attributed to the increase of NADPH supply. These results indicate that the balance of NADPH and ATP supply and consumption was achieved by enhanced carbon assimilation in the UV-A-acclimated *N. sphaeroides* CCNUC1.

A recent study reported that carbon flux through photosynthesis and central carbon metabolism shows distinct patterns among photosynthetic cells with different photosynthetic efficiency and growth rates (76). For instance, the fast-growing green alga *Chlorella ohadii* showed faster ribulose 1,5-bisphosphate (RuBP) regeneration, lower glycolysis, increased fluxes through the tricarboxylic acid cycle, and lipid synthesis, compared to the higher plants (76). In addition to the metabolic flux method, metabolomics also can provide a direct and instantaneous overview of metabolic state of the cell (77). In this study, we found that a significant decrease in intermediates (ribulose 5-phosphate and fructose 6-phosphate), a significant increase in Rubisco activity, and a significant increase in the end products (fructose and lactose) may be associated with the rapid generation and consumption of RuBP in Calvin cycle of the UV-A-acclimated *N. sphaeroides* CCNUC1. Citric acid is an allosteric inhibitor of the rate-limiting enzyme 6-phosphofructokinase in glycolysis. Therefore, the accumulation of citric acid and the decrease in pyruvate levels suggest the downregulation of the glycolysis pathway in the UV-A-acclimated *N. sphaeroides* CCNUC1 cells. Additionally, citric acid is an allosteric activator of the rate-limiting enzyme acetyl-CoA carboxylase in fatty acid biosynthesis. Therefore, a significant accumulation of both citric acid and fatty acids suggests the upregulation of lipid synthesis in the UV-A-acclimated *N. sphaeroides* CCNUC1 cells. Therefore, the metabolic characteristics of the UV-A-acclimated *N. sphaeroides* CCNUC1 cells are consistent with those of the fast-growing green algae.

UV-A radiation as a strategy for enhancing CO_2 sequestration

Carbon sequestration and emission reduction have attracted much attention in recent years, due to an increase in global warming. Despite being <1% of the biomass of the higher plants, cyanobacteria contribute to at least 25% of the global primary productivity (31). UV-A radiation has been reported to act as an energy source to directly drive photosynthetic CO_2 fixation and primary productivity of some large-sized algae under low-light or fluctuation-light conditions (9, 17, 20, 21). For instance, *in situ* carbon fixation measurements revealed that under 21.4 W m^{-2} UV-A alone, the carbon assimilation of microplankton (>20 µm) was up to 1.01 µg C (µg Chl $a^{-1}h^{-1}$) (17, 20, 21). The present study further reveals UV-A radiation could promote biomass production of *N. sphaeroides* CCNUC1 by upregulating of NADP pool with increased PSI abundance, CEF, and energy-storing carbon metabolism. Therefore, based on the novel insight into UV-A-mediated photosynthetic acclimation, UV-A radiation could be considered to be a strategy of optimizing light absorption capacity and enhancing CO_2 sequestration in the frame of a future CO_2 neutral, circular, and sustainable bioeconomy.

MATERIALS AND METHODS

Materials and culture conditions

N. sphaeroides CCNUC1 samples were collected from Hefeng County (Hubei Province, People's Republic of China), and its genome was sequenced and annotated in our previous study (38). Axenic *N. sphaeroides* CCNUC1 cultures were incubated in a nitrogen-free $BG11_0$ medium at 25°C and aerated with filtered air (0.22 µm, Millipore).

The cultures were subjected to 20 µmol photons m^{-2} s^{-1} (4.35 W m^{-2}) PAR emitted by pure white T5 LED tubes (78). The PAR intensity was measured with a quantum sensor (QRT1, Hansatech Instruments Ltd., King's Lynn, Norfolk, UK). UV-A radiation was supplied by a fluorescent UV-A lamp (365-nm UV emission peak; TL 60W/10RS; Philips, Cologne, Germany), and UV-A intensity was measured with a digital UV irradiance meter (LS125, Linshang Technology Co., Ltd., Shenzhen, China). The emission spectrum of light sources for PAR and UV-A radiation was measured with a QE65pro spectrometer (Ocean Optics Inc., Dunedin, Florida, USA) (Fig. S7). Samples were cultivated in a quartz conical flask for UV-A and PAR treatments, and samples cultured without UV-A radiation were used as the control. Since the PAR from the UV-A lamp did not affect the growth of *N. sphaeroides* CCNUC1 (Fig. S8), compared to the low visible light alone (4.35 W m^{-2}), the UV-A-mediated positive effect in the present study was attributed to UV-A (10 W m^{-2}) rather than the PAR from the UV-A lamp. The UV-A intensity was set to 5–20 W m^{-2}, according to the diurnal changes of the UV-A intensity on the Hubei Normal University campus (Huangshi, China; 30.23°N, 115.07°E), which ranged from 0 to 25 W m^{-2} on 20 January (cloudy) 2024 and 25 September (sunny), 27 September (cloudy), and 28 September (rainy) 2023 (Fig. S9). Trichomes of *N. sphaeroides* CCNUC1 were obtained from dispersed exponentially grown colonies (1- to 2-mm diameter) using a sterilized glass homogenizer, as reported previously (79). Free trichomes with the inoculi of 10 µg L^{-1} Chl a were used for the subsequent experiments.

Growth measurement

The samples were collected and extracted with 100% methanol overnight at 4°C. The methanol extracts were scanned at 200–800 nm using a spectrophotometer (Ultrospec 4300pro; GE Healthcare, England). The Chl a concentration was calculated as mentioned in a previous study (80). The specific growth rate (μ) was calculated as follows:

$$\mu = (\ln X_2 - \ln X_1)/(T_2 - T_1),$$

where X_1 and X_2 are Chl a contents at times T_1 and T_2, respectively.

The dry weight (DW) was measured after each sample was heated at 105°C until constant weight.

Photosynthetic oxygen evolution measurement

P–I response curves were generated to determine α and photosynthetic capacity (81). The samples were collected and then resuspended in fresh $BG11_0$ medium buffered with 25-mM bis-tris propane (pH 8.0) and supplemented with 2-mM sodium bicarbonate to avoid carbon limitation. The photosynthetic oxygen evolution was monitored using a Clark-type oxygen electrode (Chlorolab 2, Hansatech Instruments Ltd., Norfolk, UK) at 25°C under 11 gradients of light intensity from 0 to 915 µmol photons m^{-2} s^{-1} (3–5 min for each light intensity). Photosynthetic activity was calculated according to Henley (81), as follows:

$$\mathrm{P} = \mathrm{P_{max}} \times \tanh(\alpha \times \mathrm{I}/\mathrm{P_{max}}) + \mathrm{R_d},$$

where I is the irradiance, P is the photosynthetic activity at a specific irradiance, P_{max} is the photosynthetic capacity, α is the photosynthetic efficiency, and R_d is the dark respiration.

The PSII activity from H_2O (electron donor) to *p*-benzoquinone (*p*-BQ; electron acceptor) was determined at 550 µmol photons m^{-2} s^{-1} in the presence of 1-mM *p*-BQ and 1-mM potassium ferricyanide.

Chl fluorescence measurements

Chl fluorescence was measured using a Dual-PAM-100 (Heinz Walz, Germany). After dark adaptation for 10 min, light response was assessed under 10 gradients (20 s each) of light intensity from 29 to 1,197 µmol photons m^{-2} s^{-1}. Thereafter, 20-µM DCMU was added to the sample to obtain the maximal fluorescence yield ($F_{m\mathrm{DCMU}}$) (82). The fluorescence parameters, F_v/F_m, *qP*, and Y(II), were calculated according to Campbell et al. (82), as follows:

$$\mathrm{F_v/F_m} = (\mathrm{F_{mDCMU}} - \mathrm{F_o})/\mathrm{F_{mDCMU}},$$

$$\mathrm{qP} = (\mathrm{F_m}' - \mathrm{F_s})/(\mathrm{F_m}' - \mathrm{F_o}'),$$

$$\mathrm{Y(II)} = (\mathrm{F_m}' - \mathrm{F_s})/(\mathrm{F_m}'),$$

where F_o is the minimum fluorescence in the dark-adapted state, F_s is the steady-state fluorescence in light, F_o' is the light-adapted state constant fluorescence yield evaluated following a far-red illumination, and F_m' and $F_{m\mathrm{DCMU}}$ are maximum fluorescence values upon illumination by a saturation pulse (4,000 µmol photons m^{-2} s^{-1}, 700 ms) in the light-adapted state and in the presence of DCMU, respectively (82–84).

Chl fluorescence decay was measured after excitation with a saturating single turnover flash with a sampling rate of 2.5 µs. Decay curves were fitted by a sum of two exponential decay functions (0–20 ms, fast and slow phases) (40, 85).

P700 redox kinetic assay

Pm was measured following the method described by Klughammer and Schreiber (86). Measurements were conducted by monitoring absorbance changes at 830 and 875 nm (as a reference) using a DUAL-PAM-100 measuring system (Walz, Germany) with an ED-101US/MD emitter detector unit. Cell samples were collected by centrifugation at 4,000 *g* for 10 min at 4°C, then transferred to filter paper to remove the surface water, and weighed (0.08 g) for subsequent analysis. The cells were evenly attached to the wall of the quartz cuvette and dark-adapted for 10 min. Thereafter, the samples were subjected to far-red pre-illumination for 10 s, and the Pm was determined under the application of a saturation pulse (4,000 µmol photons m^{-2} s^{-1}, 700 ms). Pm represents the maximal change in the P700 signal upon its quantitative transformation from a fully reduced state to a fully oxidized state.

The $P700^+$ dark reduction kinetics were used to determine the CEF, following methods described by Shikanai et al. (87) and Dai et al. (88) with slight modifications. Briefly, the P700 was oxidized by far-red light (maximum at 720 nm) for 10 s in the presence of 20-µM DCMU, and the subsequent re-reduction of $P700^+$ in the dark was monitored. Considering the complexity of electron flow for reducing $P700^+$ in cyanobacteria (89, 90), we used MV (2 mM) to block the CEF (41). The difference between $P700^+$ re-reduction in the presence and absence of MV was used to determine the CEF (39, 91).

NADPH fluorescence measurement

NADPH fluorescence was measured following the method described by Mi et al. (43) and Kauny and Sétif (92). Measurements were conducted using a Walz DUAL-PAM 100 with a DUAL-ENADPH emitter unit and a standard DUAL-DR detector unit (Walz). The emitter and detector units were mounted perpendicular to each other. Cell samples (0.08-g fresh weight) were evenly attached to the wall of the quartz cuvette at 25°C and dark-adapted for 10 min. A saturating actinic light (380 µmol photons m^{-2} s^{-1}) was generated by A Chip-On-Board LED Array cone (635-nm peak emission; High-Power-LED-Lamp, Walz).

A diluted ethanolic solution of Lumogen F Violet was used to stabilize the NADPH detector–emitter system. Lumogen F Violet emits blue fluorescence upon excitation

with 365-nm wavelength as an analogy to NADPH fluorescence. The coarse and fine amplifications were adjusted to align the background reading to 0. Biological samples were then used to determine the amplification readings required to obtain valid readings. The cells were illuminated repetitively (15-s light/10-s dark intervals), and the values were calculated as an average of 10 dark–light–dark cycles.

Western blot assay

Western blot assay was performed as described previously (39). Briefly, the cell samples were pulverized in liquid N_2 and suspended in ice-cold isolation buffer [50-mM 2-(N-morpholino)ethanesulfonic acid–sodium hydroxide (pH 6.5), 25% glycerol, 10-mM magnesium chloride, 5-mM calcium chloride, and 1-mM phenylmethylsulfonyl fluoride]. The samples were then ruptured with an ultrasonic cell disruptor (Scientz-IID, Ningbo, China) in an ice bath for 10 min at 30% peak amplitude. Cell debris and unbroken cells were removed by centrifugation at 4,000 *g* for 10 min at 4°C, and the membranes (thylakoids and inner and outer cell membranes) were separated by ultracentrifugation at 40,000 *g* for 60 min at 4°C (OptimaMAX, Beckman, USA). The membranes obtained were resuspended in an ice-cold isolation buffer and subjected to Western blot analysis using a standard protocol. Briefly, equal amounts of protein samples (10 µg) were separated by 12% sodium dodecyl sulfate-polyacrylamide gel electrophoresis and transferred to a polyvinylidene fluoride membrane (Sigma, USA). Thereafter, the membranes were incubated with PS-specific primary antibodies (anti-D1, anti-CP47, anti-PsaA/B, and anti-PsaC), followed by goat anti-rabbit alkaline phosphatase antibodies. Finally, the membranes were visualized by chemiluminescence (Bio-Rad ChemiDoc XRS, Bio-Rad, USA) using nitroblue tetrazolium and 5-bromo-4-chloro-3-indolylphosphate (Amresco) as substrates. Gray levels of the Western blot bands were quantified using the ImageJ software.

NADP(H) quantification

NADP(H) quantification was conducted using a $NADP^+$/NADPH assay kit with water-soluble tetrazolium-8 (WST-8; Cat. No. S1079, Biyuntian, China). The cell samples were pulverized in liquid N_2, suspended in an extraction buffer, and heated at 60°C for 30 min. The samples were then centrifuged at 12,000 *g* for 5 min at 4°C, and the supernatant was added to a 96-well plate. To determine the size of NADP pools, the glucose-6-phosphate dehydrogenase solution was added to the wells, and the plate was incubated in the dark at 37°C for 10 min, to reduce $NADP^+$ to NADPH. Thereafter, then the WST-8 solution was added to the wells, and the plate was incubated at 37°C for 20 min to allow the formation of an orange-yellow formazan solution. Finally, the absorbance at 450 nm was measured using a microplate reader (SpectraMax i3X, Molecular Devices, Austria). The NADP(H) concentrations in samples were calculated using a standard curve.

ATP quantification

ATP quantification was conducted using the ATP Assay Kit (Cat No. S0026, Biyuntian). The samples were pulverized in liquid N_2 and suspended in an extraction buffer. Thereafter, the samples were centrifuged at 12,000 *g* for 5 min at 4°C, and the supernatant was collected. The supernatant was mixed with a firefly luciferase detection solution, and the luminescence was measured using a microplate reader (Molecular Devices). The ATP concentrations in samples were calculated using a standard curve.

Rubisco activity assay

Rubisco activity was assessed using a Rubisco Activity Assay Kit (Solarbio, Beijing, China), according to the manufacturer's instructions. Briefly, fresh samples (0.1 g) were pulverized in liquid N_2, suspended in extraction buffer (1-mL 20-mM Tris-HCl, pH = 7.5) on ice for 5 min, and centrifuged at 12,000 *g* for 5 min at 4°C. The supernatant was first mixed with RuBP solution and then mixed with 3-phosphoglycerate kinase and

glyceraldehyde-3-phosphate dehydrogenase to induce oxidation of NADH to NAD^+. The carboxylase activity of Rubisco was determined by measuring the absorbance decline rate at 340 nm (absorption peak of NADH).

Metabolite quantification by GC–MS

For metabolomic analysis, the *N. sphaeroides* CCNUC1 samples were centrifuged at 6,000 *g* for 10 min. Thereafter, the collected cells were washed thrice with phosphate-buffered saline to remove any impurities (93, 94). The samples were then immediately frozen in liquid N_2 for 20 min and stored at −80°C until further analysis. Although harvesting cells without quenching in time might result in possible metabolite interconversion, since the UV-A-acclimated and non-UV-A-acclimated cells were treated the same way, the differences between the UV-A-acclimated samples and the control should be credible in the present study. The frozen cells (50 mg) were dissolved in 80% methanol (1 mL) and chloroform (200 µL) and sonicated in an ice-water bath at 500 W in 6-s on /4-s off cycles for 3 min. 2-Chloro-L-phenylalanine (0.06 g L^{-1}, 40 µL) was added to the samples as an internal standard. The mixtures were sonicated for 20 min in an ice-water bath, incubated at −40°C for 30 min, and centrifuged at 12,000 *g* for 10 min at 4°C. Subsequently, the supernatant (400 µL) was added to a glass vial and freeze-dried using a centrifugal-freeze dryer. All samples in equal amounts were mixed as quality control (QC) samples. The QC samples were used to balance the GC–MS system before sample testing and to evaluate its stability during sample testing. Methoxylamine hydrochloride (80 µL 15 g L^{-1}, in pyridine) was added to the glass vial, and the sample was vortexed for 2 min and incubated at 37°C for 60 min to induce oxime reaction. Thereafter, N,O-bis-(trimethylsilyl)trifluoroacetamide (50 µL), hexane (20 µL), and a mixture of 10 internal standards (10 µL; C8, C9, C10, C12, C14, C16, C18, C20, C22, and C24) were added to the sample, which was vortexed vigorously for 2 min and then derivatized at 70°C for 60 min. The samples were placed at ambient temperature for 30 min before GC–MS analysis.

The derivatized samples were analyzed on an Agilent 7890B gas chromatography system coupled to an Agilent 5977 A mass selective detector (Agilent, CA, USA). A DB-5MS-fused silica capillary column (30 m × 0.25 mm × 0.25 µm; Agilent) was used to separate the derivatives. Helium (>99.999%) was used as the carrier gas at a constant flow rate of 1 mL min^{-1}. The oven temperature was initially set to 60°C (held for 0.5 min); then ramped four times to 125°C at 8°C min^{-1}, 210°C at 8°C min^{-1}, 270°C at 15°C min^{-1}, and 305°C at 20°C min^{-1}; and finally held at 305°C for 5 min. The injection volume was 1 µL. The injector was used in the spitless mode and maintained at 260°C. The temperatures of the MS quadrupole and ion source (electron impact) were set to 150°C and 230°C, respectively. The collision energy was set to 70 eV. Mass data were acquired in the full-scan mode (*m/z* 50–500), and the solvent delay time was set to 5 min. The QCs were injected at regular intervals (every 10 samples) throughout the analytical run to provide a set of data from which repeatability can be assessed.

Multivariate statistical analysis for metabolomics data

OPLS-DA was performed on the GC–MS data using the OECloud tool (https://cloud.oebiotech.cn/task/). Seven-fold cross-validation and 200 response permutation tests were conducted to prevent overfitting and to evaluate the quality of the model. VIP values obtained from the OPLS-DA model were used to rank the overall contribution of each variable on group discrimination. A two-tailed Student's *t*-test was used to obtain significantly differential metabolites (VIP > 1.0 and *P*-value < 0.05) (95, 96). Metabolites were classified by chemical taxonomy according to the Human Metabolome Database (www.hmdb.ca).

Statistical analysis

Statistical analysis of all the data (except GC–MS data) was performed using SPSS v17.0. Significant differences between the UV-A-acclimated and control samples were

compared by *t*-test. Additionally, statistical significance was determined by one-way analysis of variance and Tukey's HSD test.

ACKNOWLEDGMENTS

This study was funded by the National Natural Science Foundation of China (grant number 32100310), the Nature Science Foundation of Hubei Province (grant number 2022CFD076), and the Scientific Research Project of Hubei Education Department (grant number D20202501 and T2022028).

AUTHOR AFFILIATIONS

[1]Hubei Key Laboratory of Edible Wild Plants Conservation and Utilization, Hubei Normal University, Huangshi, Hubei, China
[2]Hubei Key Laboratory of Quality and Safety of Traditional Chinese Medicine Health Food, Jing Brand Co., Ltd., Daye, Hubei, China
[3]State Key Laboratory of Marine Environmental Science, Xiamen University, Xiamen, Fujian, China

AUTHOR ORCIDs

Zhen Chen http://orcid.org/0000-0002-9443-0735
Xiong-Wen Chen http://orcid.org/0000-0001-6129-1444

FUNDING

Funder	Grant(s)	Author(s)
MOST | National Natural Science Foundation of China (NSFC)	32100310	Zhen Chen
National Natural Science Foundation of Hubei province	2022CFD076	Zhe Wang
Scientific research project of Hubei education department	D20202501	Zhen Chen
Scientific Research Foundation of Hubei Education Department	T2022028	Yuan-Liang Hu

AUTHOR CONTRIBUTIONS

Zhen Chen, Conceptualization, Data curation, Resources, Writing – original draft | Zu-Wen Yuan, Data curation, Investigation | Wei-Xin Luo, Data curation | Xun Wu, Data curation | Jin-Long Pan, Validation | Yong-Qi Yin, Validation | Hai-Chen Shao, Validation | Kui Xu, Validation | Wei-Zhi Li, Validation | Yuan-Liang Hu, Methodology | Zhe Wang, Methodology | Kun-Shan Gao, Writing – review and editing | Xiong-Wen Chen, Supervision, Writing – review and editing

ADDITIONAL FILES

The following material is available online.

Supplemental Material

Fig. S1-S9 (AEM02110-23-s0001.docx). Supplemental figures.
Table S1 (AEM02110-23-s0002.xlsx). Supplemental table.

REFERENCES

1. Coohill TP. 1989. Ultraviolet action spectra (280 nM to 380 nM) and solar effectiveness spectra for higher plants. Photochem Photobiol 50:451–457. https://doi.org/10.1111/j.1751-1097.1989.tb05549.x
2. Frederick JE. 1993. Ultraviolet sunlight reaching the earth's surface: a review of recent research. Photochem Photobiol 57:175–178. https://doi.org/10.1111/j.1751-1097.1993.tb02274.x
3. Xu J, Gao K. 2010. UV-A enhanced growth and UV-B induced positive effects in the recovery of photochemical yield in *Gracilaria lemaneiformis* (Rhodophyta). J Photochem Photobiol B 100:117–122. https://doi.org/10.1016/j.jphotobiol.2010.05.010

4. Kerr JB, McElroy CT. 1993. Evidence for large upward trends of ultraviolet-B radiation linked to ozone depletion. Science 262:1032–1034. https://doi.org/10.1126/science.262.5136.1032
5. Takahashi S, Milward SE, Yamori W, Evans JR, Hillier W, Badger MR. 2010. The solar action spectrum of photosystem II damage. Plant Physiol 153:988–993. https://doi.org/10.1104/pp.110.155747
6. Gao Q, Garcia-Pichel F. 2011. Microbial ultraviolet sunscreens. Nat Rev Microbiol 9:791–802. https://doi.org/10.1038/nrmicro2649
7. Kataria S, Jajoo A, Guruprasad KN. 2014. Impact of increasing ultraviolet-B (UV-B) radiation on photosynthetic processes. J Photochem Photobiol B 137:55–66. https://doi.org/10.1016/j.jphotobiol.2014.02.004
8. Rastogi RP, Sinha RP, Moh SH, Lee TK, Kottuparambil S, Kim YJ, Rhee JS, Choi EM, Brown MT, Häder DP, Han T. 2014. Ultraviolet radiation and cyanobacteria. J Photochem Photobiol B 141:154–169. https://doi.org/10.1016/j.jphotobiol.2014.09.020
9. Häder DP, Williamson CE, Wängberg SÅ, Rautio M, Rose KC, Gao K, Helbling EW, Sinha RP, Worrest R. 2015. Effects of UV radiation on aquatic ecosystems and interactions with other environmental factors. Photochem Photobiol Sci 14:108–126. https://doi.org/10.1039/c4pp90035a
10. Shi C, Liu H. 2021. How plants protect themselves from ultraviolet-B radiation stress. Plant Physiol 187:1096–1103. https://doi.org/10.1093/plphys/kiab245
11. Helbling EW, Villafane V, Ferrario ME, Holm-Hansen O. 1992. Impact of natural ultraviolet radiation on rates of photosynthesis and on specific marine phytoplankton species. Mar Ecol Prog Ser 80:89–100. https://doi.org/10.3354/meps080089
12. Holm - Hansen O, Helbling EW, Lubin D. 1993. Ultraviolet radiation in Antarctica: inhibition of primary production. Photochem Photobiol58:567–570. https://doi.org/10.1111/j.1751-1097.1993.tb04933.x
13. Mc Leod GC, Kanwisher J. 1962. The quantum efficiency of photosynthesis in the ultraviolet light. Physiologia Plantarum 15:581–586. https://doi.org/10.1111/j.1399-3054.1962.tb08061.x
14. Nilawati J, Greenberg BM, Smith REH. 1997. Influence of ultraviolet radiation on growth and photosynthesis of two cold ocean diatoms. J Phycology 33:215–224. https://doi.org/10.1111/j.0022-3646.1997.00215.x
15. Barbieri ES, Villafanñ VE, Helbling EW. 2002. Experimental assessment of UV effects on temperate marine phytoplankton when exposed to variable radiation regimes. Limnol Oceanogr47:1648–1655. https://doi.org/10.4319/lo.2002.47.6.1648
16. Helbling E, Gao K, Gonçalves R, Wu H, Villafañe V. 2003. Utilization of solar UV radiation by coastal phytoplankton assemblages off SE China when exposed to fast mixing. Mar Ecol Prog Ser 259:59–66. https://doi.org/10.3354/meps259059
17. Gao K, Wu Y, Li G, Wu H, Villafañe VE, Helbling EW. 2007. Solar UV radiation drives CO_2 fixation in marine phytoplankton: a double-edged sword. Plant Physiol 144:54–59. https://doi.org/10.1104/pp.107.098491
18. Kosobryukhov AA, Lyubimov VY, Kreslavski VD. 2015. Adaptive mechanisms of photosynthetic apparatus to UV radiation, p 59–78. In Tripathi BN, Müller M (ed), Stress responses in plants. Springer, Cham, Switzerland.
19. Gao K, Häder DP. 2020. Photosynthetic performances of marine microalgae under influences of rising CO_2 and solar UV radiation, p 139–150. In Wang Q (ed), Microbial photosynthesis. Springer, Singapore.
20. Wu H, Gao K, Ma Z, Watanabe T. 2005. Effects of solar ultraviolet radiation on biomass production and pigment contents of *Spirulina platensis* in commercial operations under sunny and cloudy weather conditions. Fisheries Sci 71:454–456. https://doi.org/10.1111/j.1444-2906.2005.00984.x
21. Li G, Gao K. 2013. Cell size-dependent effects of solar UV radiation on primary production in coastal waters of the South China Sea. Estuar Coast36:728–736. https://doi.org/10.1007/s12237-013-9591-6
22. Harris DG, Zscheile FP. 1943. Effects of solvent upon absorption spectra of chlorophylls a and b; their ultraviolet absorption spectra in ether solution. Bot Gaz 104:515–527. https://doi.org/10.1086/335166
23. Halldal P. 1964. Ultraviolet action spectra of photosynthesis and photosynthetic inhibition in a green and a red alga. Physiol Plantarum 17:414–421. https://doi.org/10.1111/j.1399-3054.1964.tb08174.x
24. Lichtenthaler HK, Schweiger J. 1998. Cell wall bound ferulic acid, the major substance of the blue-green fluorescence emission of plants. J Plant Phy 152:272–282. https://doi.org/10.1016/S0176-1617(98)80142-9
25. Mantha SV, Johnson GA, Day TA. 2001. Evidence from action and fluorescence spectra that UV-induced violet-blue-green fluorescence enhances leaf photosynthesis. Photochem Photobiol 73:249–256. https://doi.org/10.1562/0031-8655(2001)073<0249:efaafs>2.0.co;2
26. Fuglevand G, Jackson JA, Jenkins GI. 1996. UV-B, UV-A, and blue light signal transduction pathways interact synergistically to regulate chalcone synthase gene expression in Arabidopsis. Plant Cell 8:2347–2357. https://doi.org/10.1105/tpc.8.12.2347
27. Lee MJ, Son JE, Oh MM. 2013. Growth and phenolic content of sowthistle grown in a closed-type plant production system with a UV-A or UV-B lamp. Hortic Environ Biotechnol 54:492–500. https://doi.org/10.1007/s13580-013-0097-8
28. Verdaguer D, Jansen MAK, Llorens L, Morales LO, Neugart S. 2017. UV-A radiation effects on higher plants: exploring the known unknown. Plant Sci 255:72–81. https://doi.org/10.1016/j.plantsci.2016.11.014
29. Agati G, Tattini M. 2010. Multiple functional roles of flavonoids in photoprotection. New Phytol 186:786–793. https://doi.org/10.1111/j.1469-8137.2010.03269.x
30. Ho MY, Soulier NT, Canniffe DP, Shen G, Bryant DA. 2017. Light regulation of pigment and photosystem biosynthesis in cyanobacteria. Curr Opin Plant Biol 37:24–33. https://doi.org/10.1016/j.pbi.2017.03.006
31. Flombaum P, Gallegos JL, Gordillo RA, Rincón J, Zabala LL, Jiao N, Karl DM, Li WKW, Lomas MW, Veneziano D, Vera CS, Vrugt JA, Martiny AC. 2013. Present and future global distributions of the marine cyanobacteria *Prochlorococcus* and *Synechococcus*. Proc Natl Acad Sci U S A 110:9824–9829. https://doi.org/10.1073/pnas.1307701110
32. Puente-Sánchez F, Arce-Rodríguez A, Oggerin M, García-Villadangos M, Moreno-Paz M, Blanco Y, Rodríguez N, Bird L, Lincoln SA, Tornos F, Prieto-Ballesteros O, Freeman KH, Pieper DH, Timmis KN, Amils R, Parro V. 2018. Viable cyanobacteria in the deep continental subsurface. Proc Natl Acad Sci U S A 115:10702–10707. https://doi.org/10.1073/pnas.1808176115
33. Hargreaves BR. 2003. Water column optics and penetration of UVR, p 59–105. In Helbling EW, Zagarese HE (ed), UV effects in aquatic organisms and ecosystems. Royal Society of Chemistry Press, London, UK.
34. Soule T, Garcia-Pichel F, Stout V. 2009. Gene expression patterns associated with the biosynthesis of the sunscreen scytonemin in *Nostoc punctiforme* ATCC 29133 in response to UV-A radiation. J Bacteriol 191:4639–4646. https://doi.org/10.1128/JB.00134-09
35. Moon Y-J, Kim SI, Chung Y-H. 2012. Sensing and responding to UV-A in cyanobacteria. Int J Mol Sci 13:16303–16332. https://doi.org/10.3390/ijms131216303
36. Zhao XM. 1765. A supplement to compendium of materia medica. Beijing: People's Medical Publishing House.
37. Qiu BS, Liu JY, Liu ZL, Liu SX. 2002. Distribution and ecology of the edible cyanobacterium GE-Xian-Mi (*Nostoc*) in rice fields of Hefeng county in China. J Appl Phycol 14:423–429. https://doi.org/10.1023/A:1022198605743
38. Chen Z, Shang J-L, Hou S, Li T, Li Q, Yang Y-W, Hess WR, Qiu B-S. 2021. Genomic and transcriptomic insights into the habitat adaptation of the diazotrophic paddy-field cyanobacterium *Nostoc sphaeroides*. Environ Microbiol 23:5802–5822. https://doi.org/10.1111/1462-2920.15521
39. Chen Z, Jiang HB, Gao KS, Qiu BS. 2020. Acclimation to low ultraviolet-B radiation increases photosystem I abundance and cyclic electron transfer with enhanced photosynthesis and growth in the cyanobacterium *Nostoc sphaeroides*. Environ Microbiol 22:183–197. https://doi.org/10.1111/1462-2920.14836
40. de Wijn R, van Gorkom HJ. 2001. Kinetics of electron transfer from Q_A to Q_B in photosystem II. Biochem 40:11912–11922. https://doi.org/10.1021/bi010852r
41. Yu L, Zhao J, Muhlenhoff U, Bryant DA, Golbeck JH. 1993. PsaE is required for *in vivo* cyclic electron flow around photosystem I in the cyanobacterium *Synechococcus* sp. Plant Physiol 103:171–180. https://doi.org/10.1104/pp.103.1.171
42. Pollak N, Dölle C, Ziegler M. 2007. The power to reduce: pyridine nucleotides—small molecules with a multitude of functions. Biochem J 402:205–218. https://doi.org/10.1042/BJ20061638

43. Mi H, Klughammer C, Schreiber U. 2000. Light-induced dynamic changes of NADPH fluorescence in *Synechocystis* PCC 6803 and its *ndhB*-defective mutant M55. Plant Cell Physiol 41:1129–1135. https://doi.org/10.1093/pcp/pcd038
44. Garcia-Pichel F, Sherry ND, Castenholz RW. 1992. Evidence for an ultraviolet sunscreen role of the extracellular pigment scytonemin in the terrestrial cyanobacterium *Chlorogloeopsis* sp. Photochem Photobiol 56:17–23. https://doi.org/10.1111/j.1751-1097.1992.tb09596.x
45. Moisan TA, Mitchell BG. 2001. UV absorption by mycosporine-like amino acid in *Phaeocystis antarctica* Karsten induced by photosynthetically available radiation. Mar Bio 138:217–227. https://doi.org/10.1007/s002270000424
46. Orellana MV, Petersen TW, Engh G. 2004. UV-excited blue autofluorescence of *Pseudo-nitzschia multiseries* (Bacillariophyceae). J Phycol 40:705–710. https://doi.org/10.1111/j.1529-8817.2004.03226.x
47. Chai MF, Chen QJ, An R, Chen YM, Chen J, Wang XC. 2005. NADK2, an *Arabidopsis chloroplastic* NAD kinase, plays a vital role in both chlorophyll synthesis and chloroplast protection. Plant Mol Biol 59:553–564. https://doi.org/10.1007/s11103-005-6802-y
48. Takahara K, Kasajima I, Takahashi H, Hashida S, Itami T, Onodera H, Toki S, Yanagisawa S, Kawai-Yamada M, Uchimiya H. 2010. Metabolome and photochemical analysis of rice plants overexpressing Arabidopsis NAD kinase gene. Plant Physiol 152:1863–1873. https://doi.org/10.1104/pp.110.153098
49. Zhou J, Zhang F, Meng H, Zhang Y, Li Y. 2016. Introducing extra NADPH consumption ability significantly increases the photosynthetic efficiency and biomass production of cyanobacteria. Metab Eng 38:217–227. https://doi.org/10.1016/j.ymben.2016.08.002
50. Ishikawa Y, Kawai-Yamada M. 2019. Physiological significance of NAD kinases in cyanobacteria. Front Plant Sci 10:847. https://doi.org/10.3389/fpls.2019.00847
51. Ji D, Li Q, Guo Y, An W, Manavski N, Meurer J, Chi W. 2022. $NADP^+$ supply adjusts the synthesis of photosystem I in Arabidopsis chloroplasts. Plant Physiol 189:2128–2143. https://doi.org/10.1093/plphys/kiac161
52. Abernathy MH, Yu J, Ma F, Liberton M, Ungerer J, Hollinshead WD, Gopalakrishnan S, He L, Maranas CD, Pakrasi HB, Allen DK, Tang YJ. 2017. Deciphering cyanobacterial phenotypes for fast photoautotrophic growth via isotopically nonstationary metabolic flux analysis. Biotechnol Biofuels 10:273. https://doi.org/10.1186/s13068-017-0958-y
53. Ungerer J, Lin PC, Chen HY, Pakrasi HB. 2018. Adjustments to photosystem stoichiometry and electron transfer proteins are key to the remarkably fast growth of the cyanobacterium *Synechococcus elongatus* UTEX. mBio 9:e02327-17. https://doi.org/10.1128/mBio.02327-17
54. Ungerer J, Wendt KE, Hendry JI, Maranas CD, Pakrasi HB. 2018. Comparative genomics reveals the molecular determinants of rapid growth of the cyanobacterium *Synechococcus elongatus* UTEX 2973. Proc Natl Acad Sci U S A 115:E11761–E11770. https://doi.org/10.1073/pnas.1814912115
55. Shimakawa G, Miyake C. 2019. What quantity of photosystem I is optimum for safe photosynthesis? Plant Physiol 179:1479–1485. https://doi.org/10.1104/pp.18.01493
56. Hihara Y, Sonoike K, Ikeuchi M. 1998. A novel gene, *pmgA*, specifically regulates photosystem stoichiometry in the cyanobacterium *Synechocystis* sp. PCC 6803 in response to high light. Plant Physiol 117:1205–1216. https://doi.org/10.1104/pp.117.4.1205
57. Ohad I, Raanan H, Keren N, Tchernov D, Kaplan A. 2010. Light-induced changes within photosystem II protects *Microcoleus* sp. in biological desert sand crusts against excess light. PLoS One 5:e11000. https://doi.org/10.1371/journal.pone.0011000
58. Salomon E, Keren N. 2011. Manganese limitation induces changes in the activity and in the organization of photosynthetic complexes in the cyanobacterium *Synechocystis* sp. strain PCC 6803. Plant Physiol 155:571–579. https://doi.org/10.1104/pp.110.164269
59. Ryan-Keogh TJ, Macey AI, Cockshutt AM, Moore CM, Bibby TS. 2012. Cyanobacterial chlorophyll-binding-protein Isia acts to increase the *in vivo* effective absorption cross section of photosystem I under iron limitation. J Phycol 48:145–154. https://doi.org/10.1111/j.1529-8817.2011.01092.x
60. Behrenfeld MJ, Milligan AJ. 2013. Photophysiological expressions of iron stress in phytoplankton. Ann Rev Mar Sci 5:217–246. https://doi.org/10.1146/annurev-marine-121211-172356
61. Murakami A, Fujita Y. 1991. Steady state of photosynthetic electron transport in cells of the cyanophyte *synechocystis* PCC 6714 having different stoichiometry between PSI and PSII: analysis of flash-induced oxidation-reduction of cytochrome *f* and P700 under steady state of photosynthesis. Plant Cell Physiol 32:213–222. https://doi.org/10.1093/oxfordjournals.pcp.a078066
62. Kopecná J, Komenda J, Bucinská L, Sobotka R. 2012. Long-term acclimation of the cyanobacterium *Synechocystis* sp. PCC 6803 to high light is accompanied by an enhanced production of chlorophyll that is preferentially channeled to trimeric photosystem I. Plant Physiol 160:2239–2250. https://doi.org/10.1104/pp.112.207274
63. Van Liere L, Walsby AE. 1982. Interactions of cyanobacteria with light, p 9–45. In Carr NG, Whitton BA (ed), The biology of cyanobacteria. Blackwell Sci Publications, Oxford.
64. Thomas DJ, Thomas J, Youderian PA, Herbert SK. 2001. Photoinhibition and light-induced cyclic electron transport in *ndhB*- and *psaE*- mutants of *Synechocystis* sp. Plant Cell Physiol 42:803–812. https://doi.org/10.1093/pcp/pce104
65. Yamori W, Shikanai T. 2016. Physiological functions of cyclic electron transport around photosystem I in sustaining photosynthesis and plant growth. Annu Rev Plant Biol 67:81–106. https://doi.org/10.1146/annurev-arplant-043015-112002
66. Shikanai T. 2007. Cyclic electron transport around photosystem I: genetic approaches. Annu Rev Plant Biol 58:199–217. https://doi.org/10.1146/annurev.arplant.58.091406.110525
67. Takahashi S, Badger MR. 2011. Photoprotection in plants: a new light on photosystem II damage. Trends Plant Sci 16:53–60. https://doi.org/10.1016/j.tplants.2010.10.001
68. Kramer DM, Evans JR. 2011. The importance of energy balance in improving photosynthetic productivity. Plant Physiol 155:70–78. https://doi.org/10.1104/pp.110.166652
69. Santos-Merino M, Torrado A, Davis GA, Röttig A, Bibby TS, Kramer DM, Ducat DC. 2021. Improved photosynthetic capacity and photosystem I oxidation via heterologous metabolism engineering in cyanobacteria. Proc Natl Acad Sci U S A 118:e2021523118. https://doi.org/10.1073/pnas.2021523118
70. Benson AA. 2002. Following the path of carbon in photosynthesis: a personal story. Photosyn Res 73:29–49. https://doi.org/10.1023/A:1020427619771
71. Guschina IA, Harwood JL. 2006. Lipids and lipid metabolism in eukaryotic algae. Prog Lipid Res 45:160–186. https://doi.org/10.1016/j.plipres.2006.01.001
72. Harwood JL, Guschina IA. 2009. The versatility of algae and their lipid metabolism. Biochimie 91:679–684. https://doi.org/10.1016/j.biochi.2008.11.004
73. Wu S, Huang A, Zhang B, Huan L, Zhao P, Lin A, Wang G. 2015. Enzyme activity highlights the importance of the oxidative pentose phosphate pathway in lipid accumulation and growth of *Phaeodactylum tricornutum* under CO_2 concentration. Biotechnol Biofuels 8:78. https://doi.org/10.1186/s13068-015-0262-7
74. Zhan M, Kan B, Dong J, Xu G, Han R, Ni Y. 2019. Metabolic engineering of *Corynebacterium glutamicum* for improved L-arginine synthesis by enhancing NADPH supply. J Ind Microbiol Biotechnol 46:45–54. https://doi.org/10.1007/s10295-018-2103-8
75. Liu B, Sun X, Liu Y, Yang M, Wang L, Li Y, Wang J. 2022. Increased NADPH supply enhances glycolysis metabolic flux and L-methionine production in *Corynebacterium glutamicum*. Foods 11:1031. https://doi.org/10.3390/foods11071031
76. Treves H, Küken A, Arrivault S, Ishihara H, Hoppe I, Erban A, Höhne M, Moraes TA, Kopka J, Szymanski J, Nikoloski Z, Stitt M. 2022. Carbon flux through photosynthesis and central carbon metabolism show distinct patterns between algae, C_3 and C_4 plants. Nat Plants 8:78–91. https://doi.org/10.1038/s41477-021-01042-5
77. Kumar R, Bohra A, Pandey AK, Pandey MK, Kumar A. 2017. Metabolomics for plant improvement: status and prospects. Front Plant Sci 8:1302. https://doi.org/10.3389/fpls.2017.01302
78. Neale PJ, Bossard P, Huot Y, Sommaruga R. 2001. Incident and *in situ* irradiance in lakes Cadagno and Lucerne: a comparison of methods and models. Aquat sci 63:250–264. https://doi.org/10.1007/s00027-001-8038-5

79. Deng Z, Hu Q, Lu F, Liu G, Hu Z. 2008. Colony development and physiological characterization of the edible blue-green alga, *Nostoc sphaeroides* (Nostocaceae, Cyanophyta). Pro Nat Sci 18:1475–1483. https://doi.org/10.1016/j.pnsc.2008.03.031
80. Lichtenthaler HK, Buschmann C. 2001. Chlorophylls and carotenoids: measurement and characterization by UV-VIS spectroscopy. Cur Prot in Food Analytical Chem 1. https://doi.org/10.1002/0471142913.faf0403s01
81. Henley WJ. 1993. Measurement and interpretation of photosynthetic light-response curves in algae in the context of photoinhibition and diel changes. J Phycology 29:729–739. https://doi.org/10.1111/j.0022-3646.1993.00729.x
82. Campbell D, Hurry V, Clarke AK, Gustafsson P, Oquist G. 1998. Chlorophyll fluorescence analysis of cyanobacterial photosynthesis and acclimation. Microbiol Mol Biol Rev 62:667–683. https://doi.org/10.1128/MMBR.62.3.667-683.1998
83. Genty B, Briantais JM, Baker NR. 1989. The relationship between the quantum yield of photosynthetic electron transport and quenching of chlorophyll fluorescence. Biochimica et Biophysica Acta (BBA) - Gen Sub 990:87–92. https://doi.org/10.1016/S0304-4165(89)80016-9
84. Klughammer C, Schreiber U. 2008. Complementary PSII quantum yields calculated from simple fluorescence parameters measured by PAM fluorometry and the saturation pulse method. PAM Appl Notes 1:27–35.
85. Leverne L, Krieger-Liszkay A. 2021. Moderate drought stress stabilizes the primary quinone acceptor Q_A and the secondary quinone acceptor Q_B in photosystem II. Physiol Plant 171:260–267. https://doi.org/10.1111/ppl.13286
86. Klughammer C, Schreiber U. 1994. An improved method, using saturating light pulses, for the determination of photosystem I quantum yield via $P700^+$-absorbance changes at 830 nm. Planta 192:261–268. https://doi.org/10.1007/BF01089043
87. Shikanai T, Endo T, Hashimoto T, Yamada Y, Asada K, Yokota A. 1998. Directed disruption of the tobacco *ndhB* gene impairs cyclic electron flow around photosystem I. Proc Natl Acad Sci U S A 95:9705–9709. https://doi.org/10.1073/pnas.95.16.9705
88. Dai H, Zhang L, Zhang J, Mi H, Ogawa T, Ma W. 2013. Identification of a cyanobacterial CRR6 protein, Slr1097, required for efficient assembly of NDH-1 complexes in *Synechocystis* sp. PCC 6803. Plant J 75:858–866. https://doi.org/10.1111/tpj.12251
89. Theune ML, Hildebrandt S, Steffen-Heins A, Bilger W, Gutekunst K, Appel J. 2021. *In-vivo* quantiffcation of electron flow through photosystem I – cyclic electron transport makes up about 35% in a cyanobacterium. Biochim Biophys Acta Bioenerg 1862:148353. https://doi.org/10.1016/j.bbabio.2020.148353
90. Kusama S, Miyake C, Nakanishi S, Shimakawa G. 2022. Dissection of respiratory and cyclic electron transport in *Synechocystis* sp. J Plant Res 135:555–564. https://doi.org/10.1007/s10265-022-01401-z
91. Alric J, Lavergne J, Rappaport F. 2010. Redox and ATP control of photosynthetic cyclic electron flow in *Chlamydomonas reinhardtii* (I) aerobic conditions. Biochim Biophys Acta 1797:44–51. https://doi.org/10.1016/j.bbabio.2009.07.009
92. Kauny J, Sétif P. 2014. NADPH fluorescence in the cyanobacterium *Synechocystis* sp. PCC 6803: a versatile probe for *in vivo* measurements of rates, yields and pools. Biochim Biophys Acta 1837:792–801. https://doi.org/10.1016/j.bbabio.2014.01.009
93. Chen S, Shi N, Huang M, Tan X, Yan X, Wang A, Huang Y, Ji R, Zhou D, Zhu YG, Keller AA, Gardea-Torresdey JL, White JC, Zhao L. 2021. MoS_2 nanosheets–cyanobacteria interaction: reprogrammed carbon and nitrogen metabolism. ACS Nano 15:16344–16356. https://doi.org/10.1021/acsnano.1c05656
94. Huang M, Keller AA, Wang X, Tian L, Wu B, Ji R, Zhao L. 2020. Low concentrations of silver nanoparticles and silver ions perturb the antioxidant defense system and nitrogen metabolism in N_2-fixing cyanobacteria. Environ Sci Technol 54:15996–16005. https://doi.org/10.1021/acs.est.0c05300
95. Bylesjö M, Rantalainen M, Cloarec O, Nicholson JK, Holmes E, Trygg J. 2006. OPLS discriminant analysis: combining the strengths of PLS-DA and SIMCA classification. J Chemometrics 20:341–351. https://doi.org/10.1002/cem.1006
96. Worley B, Powers R. 2013. Multivariate analysis in metabolomics. Curr Metabolomics 1:92–107. https://doi.org/10.2174/2213235X11301010092